Applied Thermal Engineering 298 (2026) 131094

Contents lists available at ScienceDirect

Applied Thermal Engineering

journal homepage: www.elsevier.com/locate/ate

Research Paper

Multiscale Thermal Modelling of Integrated Motor Drives with PCB-Embedded SiC Power Devices

Mattia Grespan [a,*], Sergio Busquets-Monge [b], Elisabet Mas de les Valls [b], Salvador Alepuz [c], Mariana Raya [d], Xavier Jordà [d], Davide Barater [e], Diego Angeli [f]

[a] Centro Interdipartimentale H2.MO.RE, Università di Modena e Reggio Emilia, via Università 4, 41121, Modena, Italy
[b] Universitat Politècnica de Catalunya, Carrer de Jordi Girona 31, 08034, Barcelona, Spain
[c] Tecnocampus, Universitat Pompeu Fabra, Carrer Ernest Lluch 32, 08330, Matarò, Spain
[d] Institut de Microelectrònica de Barcelona, Carrer dels Til·lers, 08193, Barcelona, Spain
[e] Dipartimento di Ingegneria "Enzo Ferrari", Università di Modena e Reggio Emilia, Via P. Vivarelli 10, 41125, Modena, Italy
[f] Centro Interdipartimentale EN&TECH, Università di Modena e Reggio Emilia, Piazzale Europa 1, 42124, Reggio Emilia, Italy

ARTICLE INFO

Keywords:
Integrated motor drive
Hairpin windings
Multilevel power converter
Switching cell array
PCB-embedded SiC power devices
LPTN
CFD

ABSTRACT

Integrated motor drives are frequently employed in vehicles and aircraft due to their superior power density and efficiency in comparison to separate motors and drives. These advantages are achieved through the tight integration of the electric motor with the power and control electronics within a single housing and cooling system. The latter requires careful design and consideration to ensure safe and reliable operation of both the motor and the power converter. This paper focuses on the thermal analysis of a novel integrated motor drive design, featuring PCB-embedded SiC MOSFETs within a multilevel switching cell array power converter. This architecture avoids the thermal limitations of conventionally packaged power devices. Three multiscale models based on lumped parameter thermal networks, with varying degrees of spatial resolution, are developed. Computational Fluid Dynamics and Finite Element models are employed to evaluate the most relevant heat sources and thermal resistances. Predicted winding temperatures ranged from 106 °C to 132 °C, all well below the 180 °C limit set by the insulation class, underscoring the effectiveness of the proposed design. The overall temperature-corrected electrical efficiency reached 95.4%. The results presented in this work thus highlight the potential of PCB-embedded power devices to improve the integration and thermal management of integrated motor drives. Finally, numerical results from the three multiscale models are compared, highlighting the advantages and limitations of each approach in real-world design scenarios. Among the three thermal models, the simplified single-slot 3D approach provided the best balance between modelling fidelity, computational cost, and development effort.

1. Introduction

1.1. Background

Integrated Motor Drives (IMDs) enable significant reductions in the size and weight of electric powertrains, thanks to the tight integration between electric motors and their power inverters. Furthermore, the elimination of superfluous electric components results in efficiency and reliability improvements [1]. IMDs have been employed in various industrial fields since the early 1960s, with the introduction of the first automotive alternators with rectification circuits integrated inside the case [2]. The continuous necessity to reduce the footprint of electric drives and their associated wiring has guided the design of integrated motor drives up to the development of high-power units conceived for vehicular traction [3]. In this field, light and compact power units are particularly sought after, as the freed up space can allow for better ergonomics and larger battery packs, with the resulting range increase.

In high-power IMDs, such as those used in electric vehicles, thermal management represents a major challenge, particularly for the power electronic devices, which produce large heat fluxes due to their high degree of miniaturisation [4], while simultaneously being exposed to the heat produced by the motor. Thus, thermal management must be addressed from the earliest stages of IMD design by means of simulation tools capable of producing accurate and fast temperature evaluations. Compared to standalone electric machines, which are discussed extensively in the literature, integrated motor drives present further

* Corresponding author.
E-mail address: mattia.grespan@unimore.it (M. Grespan).

https://doi.org/10.1016/j.applthermaleng.2026.131094
Received 25 November 2025; Received in revised form 21 March 2026; Accepted 17 April 2026
Available online 20 April 2026

Nomenclature

Latin letters

A	area [m^2]
$\boldsymbol{A}$	incidence matrix [–]
c_p	specific heat [$J\,kg^{-1}\,K^{-1}$]
C	temperature constant in Eq. (11) [$°C^{-1}$]
D_h	hydraulic diameter [m]
f	frequency [Hz]
f_D	equivalent Darcy friction factor [–]
$\boldsymbol{G}$	diagonal matrix of thermal conductances [$W\,K^{-1}$]
h	height [m]
I	current intensity [A]
K_{rk}	AC/DC loss ratio [–]
l	length [m]
L	losses [W]
$\dot{m}$	mass flow rate [$kg\,s^{-1}$]
n_{par}	parallel number [–]
Nu	Nusselt number [–]
p	fluid pressure [Pa]
P	electrical power [W]
Pr	Prandtl number [–]
q''	heat flux [$W\,m^{-2}$]
$\dot{Q}$	heat [W]
$\boldsymbol{Q}$	vector of heat generation terms [W]
r	radius [m]
R	thermal resistance [$K\,W^{-1}$]
R_{el}	electrical resistance [$V\,A^{-1}$]
Re	Reynolds number [–]
S	conduction shape factor [m]
t	thickness [m]
T	temperature [K]
$\boldsymbol{T}$	vector of nodal temperatures [K]
Ta	Taylor number [–]
$\vec{u}$	fluid velocity [$m\,s^{-1}$]
U	overall heat transfer coefficient [$W\,m^{-2}\,K^{-1}$]
V	volume [m^3]
w	width [m]

Greek letters

α	temperature coefficient [$°C^{-1}$]
β	concentrated loss coefficient [–]
γ	electrical resistivity [Ω m]
η	efficiency [–]
ϑ	dimensionless temperature difference [–]
λ	thermal conductivity [$W\,m^{-1}\,K^{-1}$]
μ	dynamic viscosity [Pa s]
ν	kinematic viscosity [$m^2\,s^{-1}$]
ρ	density [$kg\,m^{-3}$]
σ	external forcing [$Pa\,m^{-1}$]
φ	angle [rad]
ω	angular velocity [$rad\,s^{-1}$]

Subscripts

2t	two channels turns
a	aluminium
adv	advective
ag	air gap
b	bulk
bi	bidirectional
c	conductor
ch	channel
cmp	component
cn	converter
co	contact
conv	convective
cr	core
cu	copper
e	enamel
ex	excess
ext	external
fd	fully developed
fp	flat plate
I	inlet
int	internal
m	magnet
mo	motor
O	outlet
p	paper
rs	resin
s	stator
sh	short
sl	slot
ss	stator section
t	turbulent
ta	tall
w	winding

complexity due to the presence of power electronic devices, which are thermally coupled to the electric machine. In this work, a novel integrated motor drive design, featuring PCB-embedded SiC MOSFETs in a multilevel switching cell array power converter is investigated, with a focus on thermal management.

1.2. IMD architectures and thermal management

Integrated motor drives are continuously evolving, with new architectures being developed to meet the increasing demand for compact and efficient drive systems. Wang et al. [5] investigated the thermal management of a low-power 1.0 kW six-phase IMD, where Silicon (Si) power devices were mounted on the rear cover of the motor. A similar architecture was investigated in [6], where a Computational Fluid Dynamics (CFD) model was developed to evaluate the incident air flow provided by rotor-mounted fans. Abebe et al. [7] compared the thermal management of several IMD configurations using Finite Element Analysis (FEA). The authors concluded that the position and mounting mechanism used for the power electronic devices has a large impact on the overall thermal management. Therefore, each individual IMD configuration requires a detailed thermal analysis. Furthermore, [7] provides examples of the use of Silicon Carbide (SiC) semiconductors, which are part of the family of Wide Bandgap (WBG) power devices. Compared to traditional Silicon (Si) semiconductors, these devices generate lower losses due to their thinner structure, even at high voltage levels, and offer improved performance at high temperatures and switching frequencies [8]. Consequently, the use of WBG devices helps to mitigate the thermal management constraints associated with IMDs [1], as they can operate continuously at very high temperatures and are therefore less sensitive to the heat generated by the electric motor. Examples of IMD architectures employing WBG devices are available in the literature, including the aforementioned SiC MOSFETs [9] and Gallium Nitride (GaN) devices [10], which excel in high frequency operation. However, in all these applications, WBG devices are implemented as individually packaged power modules, each with its own case. This packaging architecture represents major limitations in terms of integration and thermal management, as the materials

making up the case must be able to withstand high-temperature operation [1]. Given the variety of possible IMD configurations, the different types of power semiconductors, and the resulting thermal constraints, detailed thermal analyses are essential for the design and validation of new integrated motor drive systems.

1.3. Modelling approaches

Most thermal modelling approaches adopted for IMDs stem from methods originally developed for electric machines, which are reviewed briefly in the following. The thermal analysis of electric motors is often performed by means of Lumped Parameters Thermal Networks (LPTNs), thanks to their flexibility, ease of implementation, and low computational cost when compared with higher order methods such as FEA or CFD. In LPTNs the physical domain is divided into regions, each defined by a temperature node. These nodes are connected by thermal resistances that model the heat transfer mechanisms and paths between regions. This technique can be used to obtain simple models formed by a handful of nodes and resistances, or more complex implementations based on large and intricate networks of thermal resistances.

Kotnik [11] developed one of the first LPTN-based model for electric machines, which was focused on the analysis of non-ventilated machines. Contemporary modelling schemes involving reduced-order thermal models are based on the pioneering work by Mellor, Roberts, and Turner [12], who proposed a generalised approach for the representation of the internals of electric motors using equivalent hollow cylindrical segments. Thermal resistances were computed by considering nominal geometric parameters and constant heat transfer coefficients, and the overall methodology was validated using experimental data on three air-cooled induction motors. Several authors have built upon the base approach presented by Mellor et al. by proposing thermal models developed for different electric motor topologies, including induction motors [13–16] and high-speed synchronous machines [17], demonstrating the flexibility and accuracy of this approach across wide range of applications. El-Refaie et al. [18] and Ponomarev et al. [19] compared modelling methodologies based on LPTN, FEA, and CFD, and found a good agreement between the different sets of numerical results. These findings highlight the strengths of the LPTN models as accurate and fast predictive tools that can be very useful in rapidly evaluating initial machine designs.

Some authors have attempted to further simplify LPTN models by reducing the number of temperature nodes included in the network, in order to reduce development and computational time, without sacrificing accuracy [20–23]. In these works the accuracy of the reduced LPTNs was enhanced through parameter identification procedures based on experimental data. While these simplified thermal models may seem very attractive due to their straightforward implementation, their possible reliance upon parameter identification methods based on experimental data may severely limit their generality, and the extensive experimental campaigns involved may considerably drive up development costs.

The accuracy and fidelity of numerical results provided by LPTNs can be improved by coupling reduced-order models with higher-order methods as CFD and FEA. The former is usually employed to derive heat transfer coefficients in the air gap [24], end winding region, and in the cooling jacket [19,25–27]. Instead, the latter is used to obtain accurate estimates about the losses generated in the windings, iron laminations, and magnets, if present [28–31].

Over the years, several interesting variants of the original LPTN approach proposed by Mellor et al. [12] have been proposed. Dajaku and Gerling [32] developed an alternative thermal network model for a permanent magnet machine, with the inclusion of compensation thermal elements. These network entities allow for the correct evaluation of the temperature rise in regions with distributed heat generation, without having to perform a fitting procedure. These concepts are discussed extensively in [33,34]. A comparison with numerical results obtained from a finite element analysis showed that using this improved modelling approach leads to a better temperature prediction in the windings and teeth.

Similarly to electric motors, the thermal analysis of power electronic devices is usually addressed by means of thermal networks [35], where thermal resistances and capacitance are derived from manufacturer data [36]. However, FEM methods are also employed to carry coupled thermal and electrical simulations [37], and when accurate thermal model of power packages under dynamic conditions are sought for [38].

These modelling methodologies allow for accurate temperature predictions for electric motors and power electronic circuits, which are treated as independent components. However, in integrated motor drives, the electric machine and power electronic devices are thermally coupled and jointly affect the overall thermal management of the system [5].

1.4. Aims and scope

Despite the large number of contributions to the thermal modelling of electric machines and power electronic devices, integrated motor drives are still rarely analysed as fully integrated devices. In particular, existing studies typically focus on conventionally packaged power electronic devices, which introduce additional thermal resistances and limit the performance and integration potentials of IMDs. Furthermore, most of the available studies treat electric machines and power electronic devices as separate subsystems, thus neglecting the thermal coupling present in highly integrated IMDs. These limitations become particularly relevant in modern electric drive applications, such as EVs, where compact and highly integrated power trains are in high demand. In this field, tightly integrated electric drives allow for greater architectural flexibility, with improvements on specific power output, passenger ergonomics, cargo capacity, and vehicle range. Thus, it is essential to investigate the thermal management of these highly integrated IMDs, taking into account all relevant heat transfer paths and the thermal coupling between components and subsystems.

The present work addresses these issues by studying the thermal management of a novel integrated motor drive design, featuring PCB-embedded (hereafter also referred to as chip-embedded) SiC MOSFETs within a multilevel switching cell array power converter [39,40]. This new architecture eliminates the conventional packaging used in individual power devices, thereby improving the electrical and thermal integration, and favouring continuous and reliable high-temperature operation. Aside from presenting thermal results on this particular IMD configuration, this paper evaluates three different modelling strategies in terms of their capabilities to predict hot-spot temperatures and to capture the thermal coupling between the electric motor and the power electronic devices. This study represents a direct improvement over modelling approaches developed for conventional architectures, which may not be suitable for highly integrated IMDs. In addition, the present results provide useful insights into the selection of modelling approaches for the design and analysis of IMDs.

The thermal management of the integrated motor drive design considered in this work is addressed by developing three multiscale thermal models with different numbers of degrees of freedom. Besides being instrumental for the thermal analysis of the present IMD, these three models allow for the assessment of the effect of spatial resolution on the temperature results and on the thermal coupling between the two subsystems. These multiscale models are based on LPTN approaches, in which the most relevant heat sources and thermal resistances are defined using FE and CFD models. In particular, FE models are employed for the definition of losses in the motor and the thermal resistances associated with power semiconductors, whereas CFD is used for the computation of the convective heat transfer resistances in the cooling jacket. The FE models were developed in previous

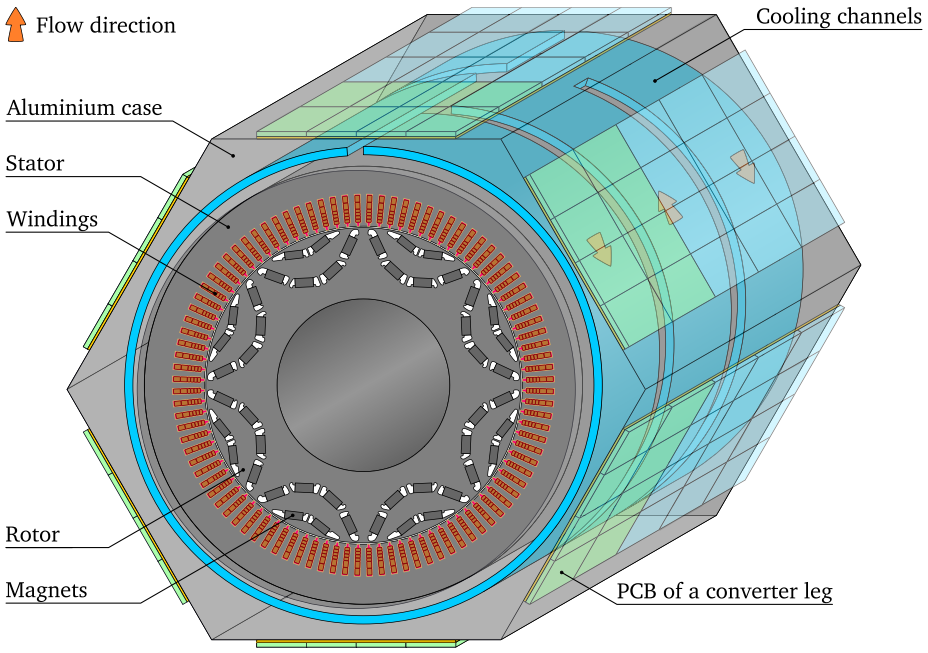

Fig. 1. Three-dimensional schematic of the integrated assembly including the traction motor, the six PCBs making up the power converter, and the hexagonal case allowing for the integration of the two systems and the cooling of all heat-generating components.

works available in the literature [41,42], while the CFD methodology represents an original contribution of the present study.

The LPTNs presented in this work are developed by using an in-house code implemented in a Python environment. While commercial tools for the thermal analysis of electric machines such as Motor-CAD are available, they are generally tailored to conventional motor designs and provide limited flexibility for novel integrated assemblies. In contrast, the proposed framework allows full control over model formulation and assumptions, allowing for the fast evaluation and optimisation of multiple IMD configurations. As a result, the proposed framework is particularly well-suited for real-world design workflows, where multiple design iterations must be rapidly evaluated with a minimal computational effort.

2. Case study

The integrated motor drive design under consideration is intended for automotive applications and consists of a six-phase synchronous motor excited by permanent magnets, and a power inverter based on a multilevel switching cell array architecture. These two devices are integrated by a shared, water-cooled, hexagonally shaped case, with the external flat surfaces serving as cold plates for the converter PCBs. This arrangement is shown in the schematic of Fig. 1, where orange arrows indicate the direction of the main flow within the cooling channels. The latter present a simple design, analogous to that of the motor case of the Nissan Leaf [43], where three circumferential channels, connected by axial crossovers, wrap around the axis of the motor. The channels have a rectangular cross-section, with a height of $h_{ch} = 5.0$ mm and a width of $w_{ch} = 40.0$ mm. The minimum thickness of the aluminium walls is $t_a = 7.0$ mm.

Fig. 2 shows the geometric details of the electric motor, in particular the stator and windings. The stator of the electric machine is made out of NO20-1200H laminated electrical steel. Its external and internal radii are $r_{s,ext} = 132.15$ mm and $r_{s,int} = 96.0$ mm, respectively. The motor presents an active length of $l_s = 140$ mm. The stator houses 96 rectangular slots, which have a width of $w_{sl} = 3.6$ mm and a height of $h_{sl} = 17.2$ mm. Each slot is lined with Kapton®-based insulating paper with a thickness of $t_p = 0.22$ mm.

At the base of the slots the paper is folded, forming a layer of insulation with a thickness of 0.44 mm. The copper windings present a hairpin arrangement, including six conductor layers of varying cross-section. This design allows for a greater fill factor compared to conventional windings. In addition, using conductors with a reduced cross-sectional area near the rotor reduces AC losses caused by proximity and skin effects. All the copper busbars have a rectangular cross-section with a width of $w_c = 2.8$ mm, while they present different heights depending on their position: the four conductors closest to the rotor have a height of $h_{c,sh} = 1.8$ mm, and the two furthest away have a height of $h_{c,ta} = 4.0$ mm. The vertical spacing between two conductors is 0.245 mm. The busbars are enamelled with a layer of Voltatex® insulating compound that has a thickness of $t_e = 0.0725$ mm, and the space between them is filled with SbTCM resin. All the materials used to insulate the windings are H-class rated, meaning that the maximum working temperature of the windings is 180 °C.

The rotor features two types of neodymium-iron-boron magnets having the same width of $w_m = 11$ mm, and heights of $h_{m,ta} = 5.5$ mm and $h_{m,sh} = 4.5$ mm. The material constituting the magnets presents a Curie temperature of 310 °C. Rotor laminations are made out of NO20-1200H steel.

The power converter presents a multilevel switching cell array architecture [39], including six main boards or legs, one for each phase. Each converter leg is composed of 8 Switching Cells (SCs) and 12 capacitors, as shown in Fig. 3. The switching cell is the basic building block of the power converter, and it is made up of a main power switch and its driver, along with the iFuse — an additional switch that deactivates the switching cell in the event of a fault. The power semiconductors are based on SiC technology, and integrated in the PCBs of the legs using chip-embedding technology. This approach consists of including semiconductor power devices in bare-die format inside the PCB stack structure, providing high levels of integration for implementing smart power modules, low profile circuitry and allowing to define the shape of the converters to specific application geometries. All these aspects are of primary interest in the study proposed in this paper. In particular, the chip-embedding technology considered in the present work, is the so-called p^2 PACK from the company Schweizer Electronic AG. This technology, with a 6-layer PCB stack, has been

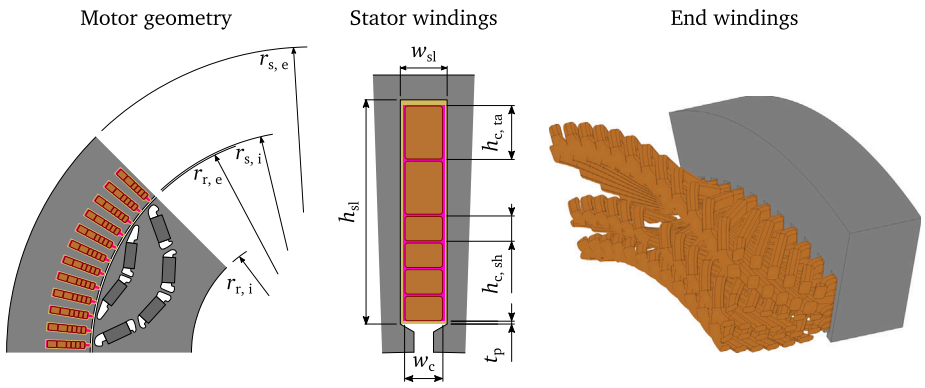

Fig. 2. Schematics of selected geometric details of the electric motor: (left) main dimensions of the stator and rotor laminations, (centre) detailed view of a stator slot along with the conductors and insulation, and (right) 3D representation of a section of the end windings.

used for the development of individual switching-cell prototypes allowing their detailed functional, electrical and thermal characterisation. Fig. 3(a) shows a schematic of the cross-section of the PCB with the embedded power devices, whereas Fig. 3(b) presents a picture of the cross-section of one of the switching-cells used for characterisation purposes [42]. The control and protection circuitry of the switching cell is assembled on the top of the PCB using SMD components. On the contrary, the power stage is embedded inside the PCB structure, including two SiC MOSFETs (for the Main Switch and iFuse functions) and a shunt resistor. The SiC MOSFETs are fixed on a Cu lead frame using a die-attach material, which is also embedded, and all electrical contacts with the embedded components are provided by the copper vias and micro-vias developed during the standard PCB manufacturing process. The adoption of SiC switches and chip embedding technology results in a working temperature limit of 200 °C at the junction of the semiconductors.

3. Numerical methods

3.1. Two-dimensional thermal model

The two-dimensional thermal model of the integrated assembly presented in this work is an improvement over the basic LPTN discussed and validated in [44]. The physical domain of the electric motor is reduced down to a basic geometry consisting of a single slot, along with the associated conductors and insulation, and half of the two adjacent teeth. This allows for a substantial reduction in the number of nodes included in the thermal model. In addition, this basic thermal network can be repeated along the circumferential and axial directions to easily extend the computational domain. The thermal model of the stator is constructed by dividing the domain into regions or zones and placing a temperature node in the middle of each heat-generating component, namely the six copper bars, the corresponding teeth sections, and the yoke of the stator. The thermal network is completed by the nodes standing for the temperatures of the air gap, the surface of the teeth, the surface of the case, and the mean bulk temperature of the cooling fluid. The arrangement of nodes and resistances making up the two-dimensional LPTN is shown in Fig. 4.

The conductive thermal resistance between a pair of nodes is evaluated by summing the contributions given by each layer of material:

$$R_{ij} = \sum_l \frac{1}{S_l\,\lambda_l}\,, \tag{1}$$

where S_l and λ_l are the conduction shape factor and thermal conductivity of a single layer, respectively. The shape factors are computed on the basis of geometric data. In the windings, flat-plate shape factors are used for the copper busbars and the insulation layers:

$$S_{\mathrm{fp}} = \frac{A}{t}\,, \tag{2}$$

where A and t are the cross-sectional area and length associated with the path taken by the heat flux, respectively. In the magnetic circuits of the stator and rotor, shape factors for radial and circumferential geometries are used. These are computed by means of the general approach proposed by Yovanovich [45]:

$$S_{\mathrm{r}} = \frac{\Delta z\,\Delta\varphi}{\ln\left(r_{\mathrm{ext}}/r_{\mathrm{int}}\right)}\,, \quad S_{\varphi} = \frac{\Delta z\,\ln\left(r_{\mathrm{ext}}/r_{\mathrm{int}}\right)}{\Delta\varphi}\,, \tag{3}$$

where Δz and $\Delta\varphi$ are the axial and circumferential spans of the considered section of solid material, respectively. The values of thermal conductivity considered for all the materials constituting the electric motor are listed in Table 1. The conductive resistances between the node of one conductor and the adjacent node of a tooth are obtained from Eq. (1), considering half a busbar, the enamel, the resin, the paper, and half of the section of tooth associated with the node under examination:

$$R_{\mathrm{ct},k} = \frac{0.5\,w_{\mathrm{c}}}{h_{\mathrm{c},k}\,l_{\mathrm{ss}}\,\lambda_{\mathrm{c}}} + \frac{t_{\mathrm{e}}}{h_{\mathrm{c},k}\,l_{\mathrm{ss}}\,\lambda_{\mathrm{e}}} + \frac{t_{\mathrm{rs}}}{h_{\mathrm{c},k}\,l_{\mathrm{ss}}\,\lambda_{\mathrm{rs}}} + \frac{t_{\mathrm{p}}}{h_{\mathrm{c},k}\,l_{\mathrm{ss}}\,\lambda_{\mathrm{p}}} + \frac{0.25\,\Delta\varphi_{\mathrm{tooth}}}{\lambda_{\mathrm{cr}}\,l_{\mathrm{ss}}\,\ln\left(r_{\mathrm{ext},k}/r_{\mathrm{int},k}\right)}\,, \tag{4}$$

where the index k refers to the considered conductor layer, starting from 0 at the layer closest to the rotor. l_{ss} stands for the portion of the active length of the motor included in the model. In this instance, it is important to underline that the value of l_{ss} does not affect temperature results, as the losses are proportional to l_{ss}, while the thermal resistances are inversely proportional to it. The thermal resistance between two adjacent conductors is obtained using an analogous approach:

$$R_{\mathrm{cc},k} = \frac{0.5\,h_{\mathrm{c},k}}{w_{\mathrm{c}}\,l_{\mathrm{ss}}\,\lambda_{\mathrm{c}}} + \frac{2\,t_{\mathrm{e}}}{w_{\mathrm{c}}\,l_{\mathrm{ss}}\,\lambda_{\mathrm{e}}} + \frac{t_{\mathrm{rs}}}{w_{\mathrm{c}}\,l_{\mathrm{ss}}\,\lambda_{\mathrm{rs}}} + \frac{0.5\,h_{\mathrm{c},k+1}}{w_{\mathrm{c}}\,l_{\mathrm{ss}}\,\lambda_{\mathrm{c}}}\,. \tag{5}$$

The other conduction resistances of the LPTN of the motor include a single layer of material and are computed according to Eq. (1), by selecting appropriate values of S and λ. The contact resistances between the stator and the internal wall of the cooling jacket are estimated by modelling heat transfer between the two uneven surfaces as heat conduction through an equivalent layer of still air. The associated thermal resistances are computed considering a flat-plate shape factor [46]:

$$R_{\mathrm{co}} = \frac{t_{\mathrm{eq}}}{\Delta\varphi\,r_{\mathrm{s,ext}}\,l_{\mathrm{ss}}\,\lambda_{\mathrm{air}}}\,, \tag{6}$$

where t_{eq} is the thickness of the equivalent layer of air between the stator and case. In this case, t_{eq} is set to 0.006 mm, as it is representative of a coupling between iron and aluminium components with loose tolerances [46], which is a conservative assumption from the point of view of thermal management.

The rotor is modelled by considering a simplified geometry consisting of two equivalent magnet layers, which are surrounded by iron laminations. The volumes of the equivalent magnets and iron sections

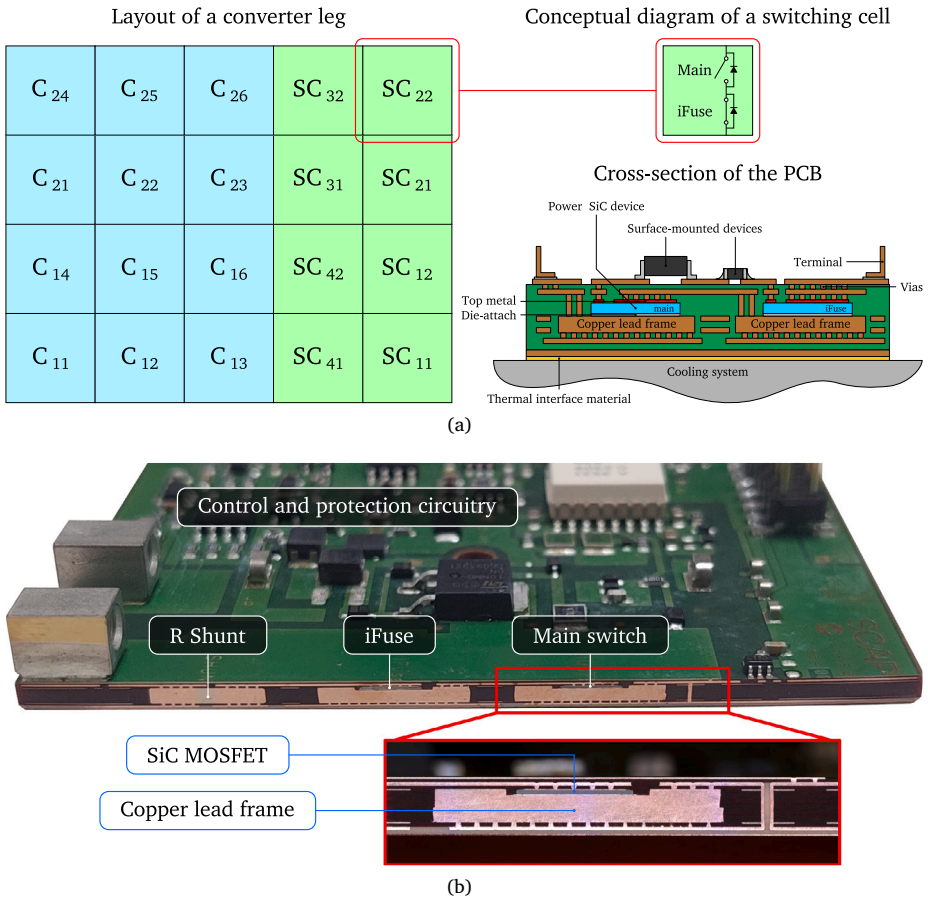

Fig. 3. (a) – Representation of the layout of one of the six converter legs, where the blocks labelled SC and C identify switching cells and capacitors, respectively. On the bottom right of the figure, a cross-section of the PCB shows the arrangement of the chip-embedded power devices. (b) – Photograph presenting a cross-section of one of the chip-embedded switching cells used for characterisation purposes [42].

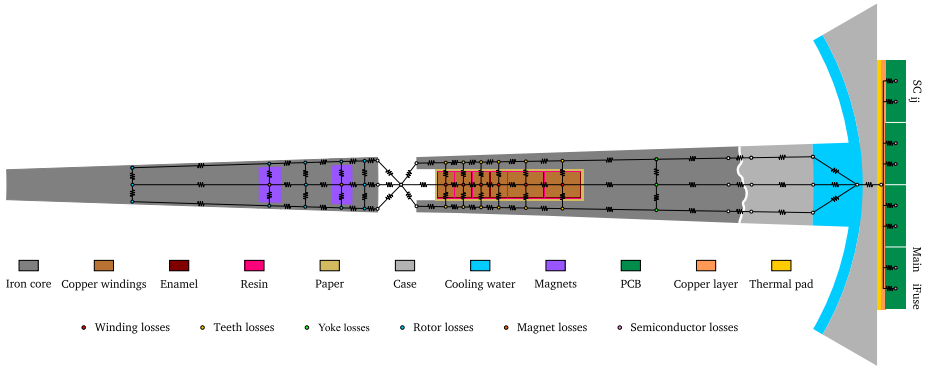

Fig. 4. Two-dimensional lumped parameter thermal network modelling the examined integrated motor drive.

are determined by uniformly distributing the volume of the actual magnets across the whole rotor. This allows for the representation of the rotor in a cylindrical reference frame at a reduced node count. The thermal resistances connecting temperature nodes in the rotor are obtained from Eq. (1) using the radial and circumferential shape factors in Eq. (3).

The convective resistances modelling heat transfer in the air gap and cooling jacket are defined as follows:

$$R_{\text{conv}} = \frac{1}{U\,A}\,, \tag{7}$$

where U is the convective heat transfer coefficient. In the air gap, U-values are obtained from the correlation by Bjorklund and Kays [47] for Taylor–Couette flows:

$$\text{Nu} = \frac{U\,D_{\text{h}}}{\lambda} = 0.35\,\text{Ta}^{0.25}\,, \tag{8}$$

where Ta is the Taylor number, which is computed on the basis of the angular velocity of the rotor ω, its radius $r_{\text{r,ext}}$, and the height of the air gap h_{ag}:

$$\text{Ta} = \frac{\omega^2\,r_{\text{r,ext}}\,h_{\text{ag}}^3}{\nu^2}. \tag{9}$$

Table 1
Thermal conductivities of the materials associated with the main components of the electric motor.

Component	Material	λ [W m^{-1} K^{-1}]
Core laminations – radial	NO20-1200H	21.0
Core laminations – axial	NO20-1200H	10.3
Winding conductors	Copper	385.0
Wire enamel	Voltatex®	0.23
Impregnation resin	SbTCM resin	3.20
Insulating paper	Kapton®	0.12
Magnets	N40UH NdFeB	6.45
Shaft	Steel	45.0
Case	Aluminium	237.0
Thermal pad	Carbon fibre	20.0

The heat transfer coefficients associated with the cooling jacket are derived from the dedicated CFD models presented in Section 3.6.

The heat generated in the conductors of the motor is modelled by means of a modified Joule heating law, which includes the temperature scaling terms proposed by Wrobel et al. [48]:

$$\dot{Q}_{c,k} = \gamma_{cu} \frac{l_{ss}}{A_{c,k}} I^2 \frac{K_{rk}\Big|_{T_{ref,cu}} - 1}{\sqrt{1+\alpha_{cu}\left(T - T_{ref,cu}\right)}} + \gamma_{cu} \frac{l_{ss}}{A_{c,k}} I^2 \left[1+\alpha_{cu}\left(T - T_{ref,cu}\right)\right] , \tag{10}$$

where γ_{cu} is the electrical resistivity of copper, which is evaluated at the reference temperature $T_{ref,cu} = 20$ °C: $\gamma_{cu} = 1.724 \times 10^{-8}$ Ω m. α_{cu} is the temperature coefficient of copper, which equates to 4.29×10^{-3} °C $^{-1}$. The K_{rk} coefficient represents the ratio between AC and DC losses of the kth conductor. In this case, the K_{rk}-values are derived from the Finite Element Analyses presented in [49,50], modelling the active section of the motor and the end windings, respectively. In these studies, a uniform winding temperature of 120 °C was considered, and the resulting values of K_{rk} are reported in the graph of Fig. 5, for all the conductor layers in the active section and end windings. These values of AC/DC loss ratio are scaled from 120 °C to 20 °C using the scaling laws in [48], so that they are scaled consistently with temperature once they are introduced in Eq. (10).

In this case, the scaling laws from [48] are used exclusively to account for temperature effects. Instead, the frequency dependence of AC losses, identified as the dominant factor compared to temperature effects [48], is modelled in full, as the K_{rk} distributions in Fig. 5 are derived from frequency-dependent, high-fidelity FE models presented in [49,50]. Moreover, the temperatures scaling laws adopted in this work have been shown to provide high accuracy for rectangular conductors at phase frequencies below 1.6 kHz, which is below the maximum operating frequency of the present IMD. Finally, the temperature scaling is applied over a limited temperature range of ±14 °C around the 120 °C baselines, as it will be shown later by the temperature results in Fig. 14. Within this range, the influence of temperature variations on AC losses is expected to be minimal. Overall, the above considerations support the use of the temperature scaling law in Eq. (10) to accurately represent temperature effects in the windings.

The losses associated with the laminations of the yoke, the teeth, the rotor, and the magnets are derived from the aforementioned FE models, and are listed in Table 2. In this case, temperature effects are not considered as they are significantly less relevant when compared to those in the copper windings. These losses are assigned to the nodes related to their respective components by treating them as uniformly distributed volumetric heat sources.

The thermal model of the power converter and external wall of the cooling jacket features a much simpler layout compared to the LPTNs of the stator and rotor. The nodes standing for the main and iFuse switches are connected in parallel to the last copper layer of the PCB through $R_j = 0.62$ °C/W, which models heat conduction between the junction of

Table 2
Losses in the core laminations and permanent magnets.

Component	Yoke	Teeth	Rotor	Magnets
Losses [W]	1028.5	848.7	290.0	7.952

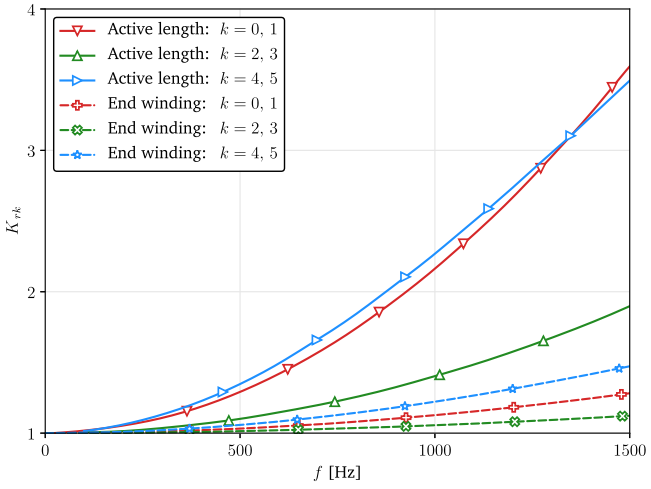

Fig. 5. Values of the AC/DC loss ratio K_{rk} as a function of frequency for all conductor layers in the active section and end windings.

the embedded semiconductors and the last copper layer of the PCB. The value of R_j is obtained from the Finite Element model of the switching cell developed by Raya et al. [42].

The PCB of the converter leg is attached to the external walls of the case by means of a conductive carbon fibre thermal pad that has a thickness of $t_{pad} = 0.4$ mm. In this case, conductive thermal interface materials can be used without causing short circuits as all semiconductors are internally insulated. The convective resistance between the cooling fluid and the external walls of the case is obtained from the CFD model presented in Section 3.6.

The switching and conduction losses associated with each power device are derived by following the procedure outlined in [51], and by considering the reference temperature $T_{ref,j} = 100$ °C. These losses are listed in Table 3, where values in red refer to conduction losses in iFuses occurring when these devices are made out of the same semiconductors used for the main switches, which are optimised for switching performance rather than pure conduction. Instead, values in green are referred to a power switch tailored for continuous conduction.

In this case, both configurations are considered to properly assess their respective benefits and drawbacks. Of course, the non-optimal layout will lead to a higher thermal load and lower converter efficiency. However, it allows for a much simpler chip embedding process, given that the same type of semiconductor is used for both the main and iFuse components in each switching cell. In contrast, the optimised configuration involves a more complex design and manufacturing, while leading to a lower thermal load. In the following, the thermal loads associated with the optimised and non-optimised switch configurations will be referred to as *best-case* and *worst-case* conditions, respectively.

All conduction losses are scaled with temperature by considering the following relation:

$$\dot{Q}_{cond}\Big|_T = \dot{Q}_{cond}\Big|_{T_{ref,j}} \left[1 + C\left(T - T_{ref,j}\right)\right] , \tag{11}$$

where C is equal to 1.429×10^{-3} °C^{-1}, and T stands for the junction temperature of the power devices, which is modelled by their respective temperature nodes.

Table 3
Conduction, switching, and total losses for each switching cell.

Component	Sub-component	L_{cond} [W]	L_{sw} [W]	L_{tot} [W]	
SC_{11}, SC_{12}, SC_{41}, SC_{42}	main	9	43	52	→ 61/54
	iFuse	9/2	0	9/2	
SC_{21}, SC_{31}	main	7	21	28	→ 35/29
	iFuse	7/1	0	7/1	
SC_{22}, SC_{32}	main	41	0	41	→ 82/49
	iFuse	41/8	0	41/8	

3.2. Three-dimensional thermal model of a single slot

The basic two-dimensional thermal model developed in Section 3.1 allows for quick evaluations of the hot-spot temperatures and overall thermal management of the IMD assembly. However, its intrinsic simplicity introduces two limitations that could potentially affect the accuracy of the resulting estimates. First, the adopted two-dimensional framework does not allow for the introduction of the losses generated in the end windings, and the computation of the temperatures in this region. Although the losses in the end windings are much lower than those observed in the active region due to reduced proximity effects, it is important to consider the thermal management of the exposed conductors on both sides of the machine, as these are not in contact with the rest of the motor and cooling system, which may result in elevated temperatures during the operation of the machine. The second significant limitation of the 2D LPTN is the assumption of a uniform coolant bulk temperature, which of course is not verified in the real system.

The drawbacks and limitations brought by the two-dimensional thermal model are addressed by extending it along the axis of the motor to derive a primitive 3D LPTN encompassing a single slot of the electric machine and a single converter leg. The arrangement of nodes and resistances constituting the thermal models of the stator and rotor is replicated three times, subdividing the domain into three axial slices, as shown in Fig. 6. This axial node layout was chosen for the following reasons. First, since the cooling jacket presents three main channels, this spatial discretisation scheme is well-suited for evaluating the coolant temperature increase along the axis of the case. Indeed, each coolant temperature node models the mean bulk temperatures of the cooling fluid over an entire turn of the channels. Second, although relatively coarse, the selected axial discretisation is considered adequate for accurately computing axial temperature gradients, despite the temperature-dependent heat generation in the windings. As previously stated, winding losses mainly depend on the phase frequency and position of each conductor and much less so on the temperature through variations in the electrical resistivity of copper. In addition, axial temperature gradients in the windings are expected to remain modest due to the hairpin architecture and the high thermal conductivity of copper compared to the other materials making up the motor. This assumption is confirmed by the limited axial temperature gradients shown later in Fig. 14. Furthermore, this three-level axial discretisation is also adopted in relevant publications on electric motors with the same architecture as the motor analysed in this work [52]. All interior nodes are connected by axial resistances that are defined on the basis of the shape factor for flat plates in Eq. (2). The end windings are modelled by considering six open-ended conductors on either side of the active section of the motor. A temperature node is positioned at the centre of each section of conductor extending from the stator. These nodes are connected to the corresponding nodes in the active section of the machine by conductive thermal resistances. The losses generated in the exposed conductors are evaluated by means of Eq. (10), using the K_{rk} coefficients derived from a 3D Finite Element model that includes the complete end winding arrangement [50]. These values are reported in the plot of Fig. 5, as a function of frequency. In this case, the K_{rk}-values are significantly lower when compared to those related to the active section of the motor, as proximity effects are almost negligible in the end windings, and AC losses are mostly influenced by the skin effect, which is produced by the conductor's own flux linkage [53]. The lateral surfaces of the end windings are assumed to be adiabatic. This is a conservative assumption as it represents the most unfavourable scenario for thermal performance, and it is also supported by previous studies on the cooling of end windings of electric motors available in the literature. The experimental tests performed by Boglietti et al. [54] showed that, for totally enclosed motors, i.e. those presenting sealed cases without openings, the airflow due to rotor rotation has a limited impact on the cooling of end windings. Specifically, rotors without end rings or fins produce a weak airflow that has little to no effect on the cooling of the end windings (up to 0.3% ΔT reduction), whereas those equipped with finned end rings can reduce the overtemperature of the windings by up to 12% from 0 to 2500 rpm, beyond which the cooling effect appears to stabilise. In contrast, motors with open housings show a much greater sensitivity to the airflow generated by the rotor, which can help to reduce winding temperatures by up to 68% [54]. Since the motor considered in this work does not present finned end rings, and it is completely sealed (vehicular application), assuming adiabatic end windings is not only a conservative assumption, but is also supported by the literature. On the other hand, in motors equipped with dedicated cooling systems for the end windings [52] or open case design such as Open Drip Proof (ODP) [54], heat transfer at the end winding surfaces becomes a determinant factor in the overall thermal performance.

The advection of thermal energy due to coolant flow within the case is modelled by connecting the nodes standing for the bulk temperature of the fluid with advective or transport thermal resistances. These are defined by considering the thermal energy balance applied to the inlet and outlet sections of a simple duct:

$$R_{adv} = \frac{\Delta T}{\dot{Q}} = \frac{T_{b,O} - T_{b,I}}{\dot{m}\, c_p \left(T_{b,O} - T_{b,I}\right)} = \frac{1}{\dot{m}\, c_p}. \tag{12}$$

R_{adv}, unlike the other thermal resistances, is not bidirectional. Specifically, it allows for heat to flow only along one direction. A close analysis of the third term of Eq. (12) reveals that R_{adv} is oriented along the direction opposite to that of the velocity vector or, in other words, it is oriented from $T_{b,o}$ (outlet) to $T_{b,i}$ (inlet). The directionality of R_{adv} is modelled by an in-line thermal diode.

The LPTN presented in Fig. 6 is used to model the complete integrated motor drive by considering several of these axial slices encompassing a single slot connected in parallel. To this end, all thermal resistances apart from advective ones are divided by the number of parallel connections n_{par}, while all losses are multiplied by it:

$$R_{ij,\,full} = \frac{R_{ij}}{n_{par}}, \quad \dot{Q}_{i,\,full} = \dot{Q}_i\, n_{par}\ , \tag{13}$$

where n_{par} is equal to the number of slots (96) for all resistances and losses associated with the motor, while it is equal to 6 for the resistances and losses associated with the power converter, as the latter presents six converter legs. These assumptions allow for the correct evaluation of the coolant temperature increase along the axial development of the cooling jacket at a reduced node count, as the losses of the complete assembly are injected into a simplified model comprising nodes and resistances associated to a single slot of the motor and a single converter leg.

3.3. Complete 3D thermal model

The basic three-dimensional model developed in Section 3.2 allows for the estimation of the average thermal behaviour of the integrated motor drive. However, this simplified 3D approach, much like the 2D LPTN, features some limitations when compared to a complete three-dimensional model. The most relevant of these is the lack of an important path of heat flow associated with the motor. Indeed, in the 2D and 3D single-slot models, heat transfer across winding layers

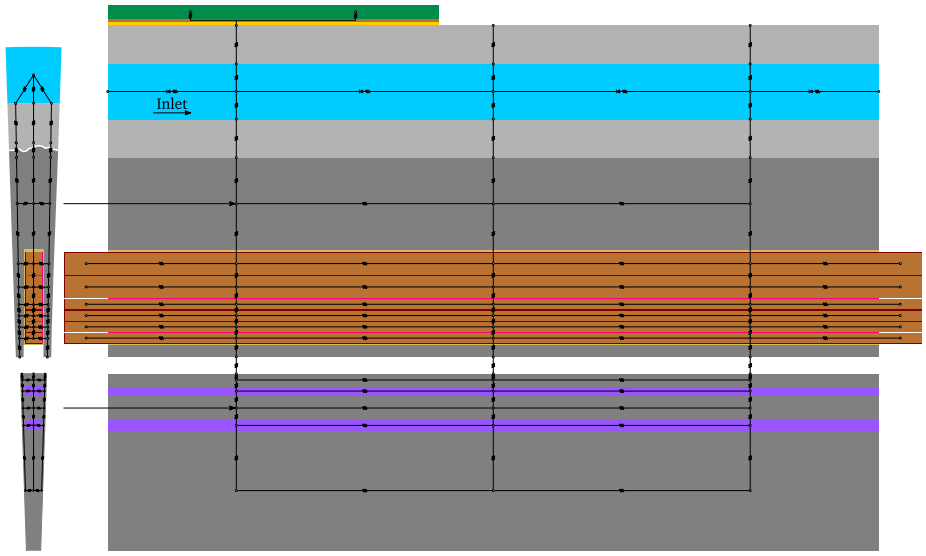

Fig. 6. Longitudinal section of the 3D LPTN of a single slot positioned at the centreline of the windings.

mainly occurs along the vertical direction through the electrical insulation layers formed by the wire enamel and the resin separating the conductors. In the actual motor, however, heat is exchanged between winding layers not only across the insulation, but also through the inter-layer connections formed by the end windings, as shown in Fig. 2. Since the thermal conductivity of copper is orders of magnitude greater than that of the other materials making up the motor, this particular heat path must be considered in the thermal model. The resulting redistribution of heat fluxes across the end winding connections leads to a reduction in the temperatures observed in the windings. This aspect will be discussed further in Section 4.2, where numerical results from both 3D LPTNs are compared.

The complete three-dimensional model of the integrated motor drive is obtained by starting from the 2D LPTN, and reproducing its arrangement of nodes and resistances 96 times along the circumferential direction and three times along the axial one. All centre-point nodes are connected by circumferential and axial resistances, which are defined on the basis of their respective conduction shape factors. By modelling the complete motor, the connections between the winding layers can now be accurately represented. The thermal connections are arranged in the same way as the electrical connections, as shown in Fig. 7. Starting from the conductor closest to the rotor, each busbar is connected to the conductor positioned one layer above it, and associated with a slot located at 12 slots away from the initial slot. The coolant temperature nodes associated with the slots are connected by advective resistances and thermal diodes, following the path of coolant within the case, as shown in Fig. 8. The sub-models for the converter boards are connected to the coolant temperature nodes of slots 0, 16, 32, 48, 64, and 80. Fig. 9 shows a schematic of a quarter of the front face of the complete 3D thermal model, where the connection between the sub-model of a converter leg and the coolant temperature node in the motor is clearly shown.

3.4. Implementation and boundary conditions

The lumped parameter thermal networks presented in this work are implemented in a Python 3 environment using an in-house-developed library for the development and analysis of reduced order models. The thermal models are defined using a modular approach, so that the basic arrangement of nodes and resistances forming the 2D model can be simply extended to form the other two networks using routines based on `for` cycles.

The thermal networks developed in the present work are solved by means of a numerical approach based on the graph theory. The arrangement of nodes and resistances that make up each thermal network is modelled as a set of nodes connected by directed branches, representing the thermal resistances. The connections between temperature nodes (i) and thermal resistances (j) are represented by the $n_i \times n_j$ incidence matrix $\boldsymbol{A}$.

$$A_{ij} = \begin{cases} +1 & \text{if resistance } j \text{ starts from node } i \\ -1 & \text{if resistance } j \text{ is bidirectional and ends at node } i \\ 0 & \text{if resistance } j \text{ is unidirectional and ends at node } i \\ 0 & \text{if resistance } j \text{ is not connected to node } i \end{cases} \tag{14}$$

The incidence matrix is then used as a basis to assemble and solve the system of algebraic equations governing the thermal network:

$$\boldsymbol{A}\,\boldsymbol{G}\,\boldsymbol{A}_{\mathbf{bi}}^{\top}\,\boldsymbol{T} = \boldsymbol{Q}\,, \tag{15}$$

where $\boldsymbol{G}$ is the diagonal matrix of thermal conductances ($G_{jj} = 1 / R_j$), $\boldsymbol{T}$ is the vector of nodal temperature values, and $\boldsymbol{Q}$ is the vector of volumetric heat generation terms. Moreover, $\boldsymbol{A}_{\mathbf{bi}}$ is an alternative form of the incidence matrix, where all thermal resistances, including the advective ones, are treated as bidirectional. Eq. (15) is solved by using an algorithm based on the LU factorisation of sparse matrices implemented in the SciPy library [55].

The boundary conditions applied to the thermal models consist of those defining the operating point of the motor, and the temperature boundary condition considered for the cooling system. The root-mean-square value of the phase current is set to 80 A, corresponding to an overall electric power of 100 kW for this particular motor. The frequency of the phase current is set to 600 Hz, leading to a shaft rotational speed of 9000 rpm, which is suited for the desired vehicular application. In the 3D models, the inlet temperature of the coolant is set to 60 °C, whereas in the 2D LPTN, the coolant temperature is set to 68.6 °C, as it corresponds to the mean bulk temperature associated with the entire system. The coolant flow rate is set to 5 l/min. The boundary conditions described herein are summarised in Table 4.

3.5. Validation of advective resistances and thermal diodes

The correct implementation of the advective resistances included in both the 3D LPTNs presented in Sections 3.2 and 3.3 is verified by comparing numerical results on the coolant bulk temperature increase, obtained by considering the boundary conditions in Table 4, with the

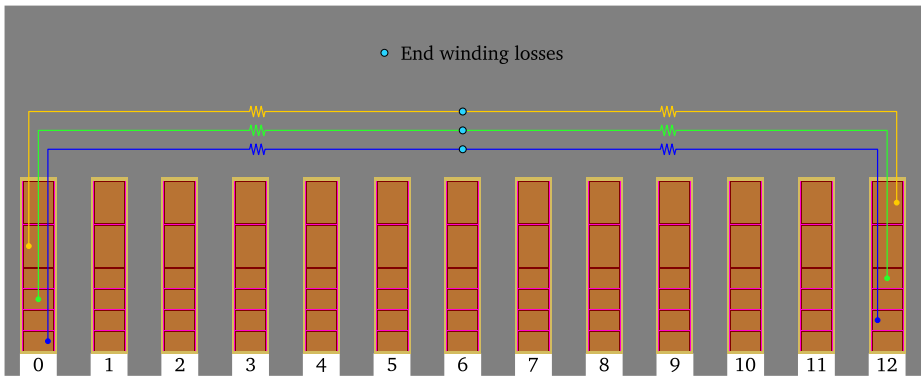

Fig. 7. Example of thermal connections between winding layers.

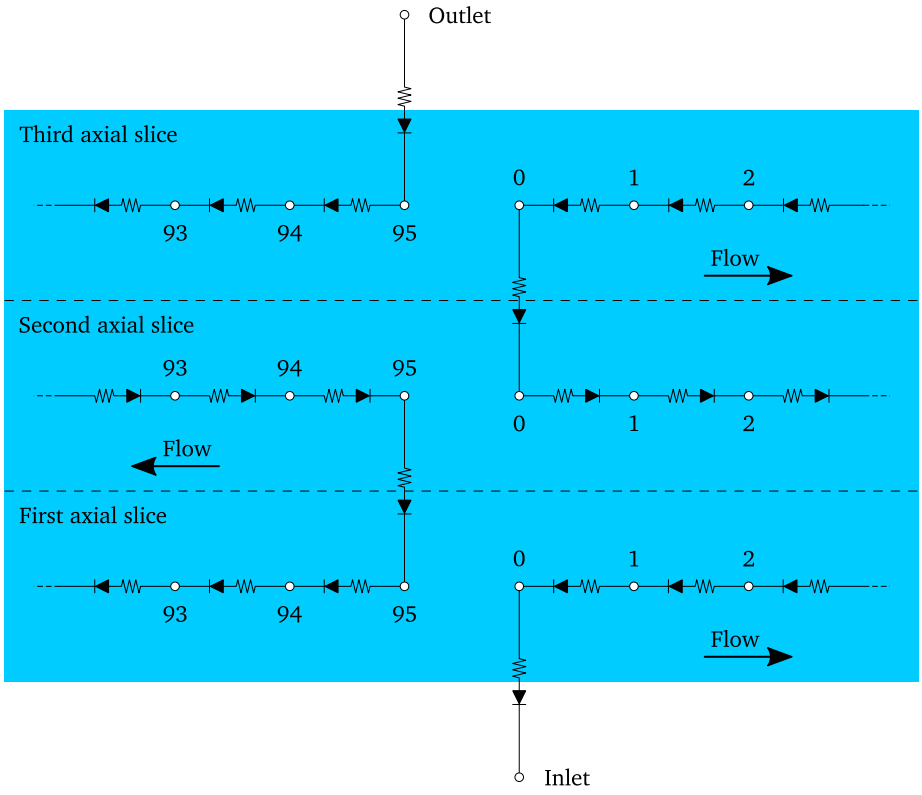

Fig. 8. Example of thermal connections between the nodes modelling the coolant bulk temperature values in the complete 3D LPTN.

Table 4
Boundary conditions applied to the thermal models developed for the integrated motor drive under examination.

Parameter	Value	Units
Phase current	80	A
Rotor speed	9000	rpm
Frequency	600	Hz
Coolant flow rate	5	l/min
Mean coolant temperature (2D model)	68.6	°C
Inlet coolant temperature (3D models)	60	°C

expected ΔT_b-value retrieved from a simple thermal energy balance applied between the inlet and outlet of the cooling jacket:

$$\Delta T_b = \frac{\dot{Q}_{tot}}{\dot{m}\, c_p}, \tag{16}$$

where $\dot{Q}_{tot}$ is the sum of all losses introduced in the model. Table 5 reports the expected values of ΔT_b, their numerical counterparts, and the difference between them. Both the 3D LPTNs are able to correctly model the coolant temperature increase. The deviations observed between the expected and numerical values result from round-off errors typical of floating-point arithmetic operations, and are negligible with respect to the temperature values.

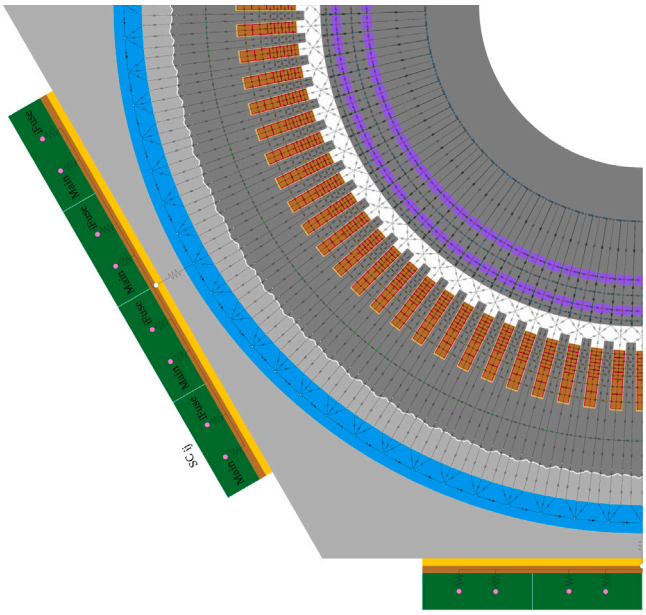

Fig. 9. Schematic of one quarter of the front face of the complete 3D LPTN of the integrated assembly, where the connections between the LPTN of the motor and those of the converter legs are clearly represented.

Table 5
Expected and numerical values of bulk temperature difference obtained from the two three-dimensional thermal models. Values in °C.

Model	Expected ΔT_b	Model ΔT_b	Deviation
3D single-slot	17.25	17.25	1.7×10^{-13}
Complete 3D	17.25	17.25	4.7×10^{-11}

3.6. Numerical model of the cooling jacket

3.6.1. Governing equations

The heat transfer coefficients associated with the internal and external walls of the cooling jacket are obtained by developing dedicated computational fluid dynamics models. Specifically, two CFD models of reduced portions of the cooling jacket are developed. The first of these models includes one-sixth of a single channel, whereas the second encompasses two complete channel turns, to investigate the effect of the 180-degree bends, shown in Fig. 1, on heat transfer effectiveness and head losses. In both cases, the problem is stated in terms of the dimensionless RANS and thermal energy equations [56]:

$$\begin{aligned} u_j^* \frac{\partial u_i^*}{\partial x_j^*} &= -\frac{\partial p^*}{\partial x_i^*} + \frac{\partial}{\partial x_j^*}\left[\left(\frac{1}{\mathrm{Re}} + \nu_t^*\right)\frac{\partial u_i^*}{\partial x_j^*}\right] + \sigma^* \\ \frac{\partial u_i^*}{\partial x_i^*} &= 0 \\ u_j^* \frac{\partial T^*}{\partial x_j^*} &= \frac{\partial}{\partial x_j^*}\left[\left(\frac{1}{\mathrm{Re}\,\mathrm{Pr}} + \frac{\nu_t^*}{\mathrm{Pr}_t}\right)\frac{\partial T^*}{\partial x_j^*}\right] \end{aligned} \tag{17}$$

where non-dimensional terms appear as starred. The temperature in the aluminium walls is determined from the steady-state heat conduction equation:

$$\frac{\partial}{\partial x_j^*}\left(\lambda_s^* \frac{\partial T^*}{\partial x_j^*}\right) = 0. \tag{18}$$

The eddy viscosity term in Eqs. (17) is computed according to the k-ω SST turbulence model [57], and by using a low-Reynolds wall treatment. The turbulent Prandtl number Pr_t is set to 0.85. The external forcing term σ^* is computed iteratively to maintain the desired flow rate at the inlet and outlet sections of the channel.

The height of the channel h_{ch} is chosen as the reference length of the problem [58]. As a result, the Reynolds and Prandtl numbers take the following forms:

$$\mathrm{Re} = \frac{\bar{u}_I\, h_{ch}}{\nu}, \quad \mathrm{Pr} = \frac{\nu}{\alpha}, \tag{19}$$

where the velocity scale $\bar{u}_I$ is the surface mean velocity over the inlet section of the channel. The non-dimensional thermal conductivity of the solid walls is defined as:

$$\lambda_s^* = \frac{\lambda_{alu}}{\lambda_{fluid}}. \tag{20}$$

3.6.2. Boundary conditions

In both CFD models, a fully developed flow solution is attained by enforcing periodic boundary conditions to all fields between the inlet and outlet patches. No-slip conditions are applied on all surfaces constituting the fluid-solid interface, where the continuity of temperature and heat fluxes is also enforced. The two heat transfer coefficients associated with the internal and external walls are retrieved by performing numerical analyses using two sets of temperature boundary conditions: an entering heat flux is imposed on the wall under examination, while the other is considered adiabatic.

3.6.3. Spatial discretisation

The numerical solution to the governing equations is obtained by means of a Finite Volume conjugate heat transfer solver, based on the SIMPLE algorithm [59], and implemented in the OpenFOAM 2206 computational toolset [60]. Advective terms are discretised using second-order upwind schemes. Central schemes featuring explicit non-orthogonality correction are used for diffusive terms instead. The computational domains are discretised by means of block-structured grids, which are smoothed using a multi-grid algorithm based on the Thomas–Middlecoff method [61], and implemented in the mesh generation tool Pointwise. Selected views of the two computational grids are shown in Fig. 10, where fluid and solid regions are highlighted.

3.6.4. Mesh sensitivity analysis

The influence of grid resolution on numerical results is assessed by developing three computational meshes of a sixth of a single channel with different cell sizes, and comparing the numerical results obtained. The coarse, intermediate, and fine computational meshes present an analogous topology, with the wall-normal spacing and mean size of the cells decreasing each time by one half from the coarse to the fine grid.

Numerical results from the three computational grids are listed in Table 6, along with the mean non-dimensional size of the cells $\overline{\Delta}^*$, the integral mean values of the dimensionless wall distance $\overline{y}^+$, and the value of the Nusselt number associated with the internal wall Nu_{int} obtained at zero grid spacing by means of Richardson's extrapolation [62], which is applied between numerical results from the intermediate and fine grids.

Numerical results do not show a convergent behaviour with respect to the mean element size: the coarse grid produces the maximum Nusselt number value, while the intermediate mesh accounts for the minimum. However, numerical results from the coarse grid may be unreliable, as the mean $\overline{y}^+$ value is well above unity, which is considered the upper limit for the use of low-Reynolds turbulence models. The fine grid produces results close to the extrapolated continuum value. In contrast, the numerical outcomes obtained from the intermediate and coarse meshes present substantial deviations with respect to each other and the fine grid. For these reasons, the results stemming from the fine grid are considered for all subsequent thermal analyses. Furthermore, the size parameters of the fine grid are also adopted for the mesh encompassing two complete channel turns.

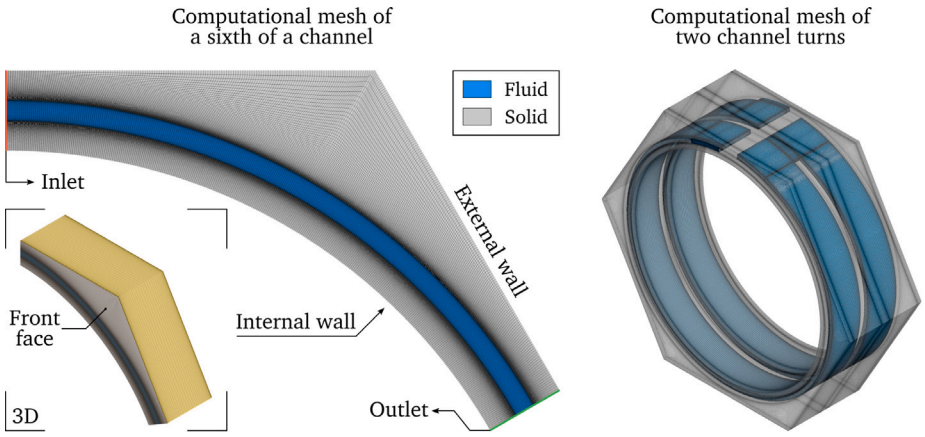

Fig. 10. Selected view of the computational meshes developed for the CFD models of a sixth of a single channel (left) and of two complete channel turns (right). In this figure, fluid and solid regions are represented in light blue and grey, respectively.

Table 6
Numerical results obtained from the coarse, medium, and fine computational grids, along with the continuum value obtained by means of Richardson's extrapolation.

	$\overline{\Delta}^{+}$	$\overline{y}^{+}$	Nu_{int}	Dev.
Coarse grid	0.1	4.7	23.6	
Intermediate grid	0.05	0.72	20.1	−14.9%
Fine grid	0.025	0.37	21.3	5.6%
Richardson's extrap.			21.7	1.7%

4. Results and discussion

4.1. Cooling jacket

Numerical flow field results associated with the cooling jacket are presented by means of contour plots of dimensionless velocity magnitude and temperature difference. The latter is defined as:

$$\vartheta = \frac{\overline{T}_{wall} - T}{\overline{T}_{wall} - \overline{T}_{b}}, \tag{21}$$

where $\overline{T}_{wall}$ stands for the integral mean temperature of the heated wall, while $\overline{T}_{b}$ is the mean bulk temperature of the cooling fluid. Fig. 11 shows examples of these contour plots, associated with a flow of glycol-based coolant at Re = 2481 and Pr = 7.0. For the one-sixth model, these are obtained on centred transversal sections of the computational domain, whereas, for the extended computational domain, a cylindrical section at half the channel height is used. The radial velocity distribution observed in Fig. 11(a) is not symmetric with respect to the centreline of the channel, due to its curvature and the effect of centrifugal forces. As a result, the boundary layer on the internal wall of the channel is much thinner compared to that on the external wall. This leads to improved heat transfer effectiveness at the internal wall as confirmed by the two temperature contours in Figs. 11(b) and 11(c). Figs. (d) and (e) show the dimensionless velocity and temperature distributions obtained from the CFD model including two complete channel turns. In this case, the velocity distribution is much less uniform than that from the one-sixth channel model, which is shown in Fig. 11(a). Near the 180-degree bends, fluid velocity increases sharply at the bend entrance, leading to the formation of large recirculation regions at the sharp corners. This flow arrangement increases the head losses and diminishes the overall heat transfer effectiveness compared to the outcomes from the one-sixth channel model. These aspects are discussed in the following.

The heat transfer effectiveness associated with the internal and external walls of the cooling jacket is expressed by the corresponding Nusselt numbers:

$$Nu = \frac{\dot{Q}\, h_{ch}}{\lambda\, A\, (\overline{T}_{wall} - \overline{T}_{b})}. \tag{22}$$

Nu-values are computed from both CFD models of the cooling jacket to evaluate the effect of the 180-degree bends on heat transfer results.

The head losses associated with the cooling channels are computed as follows. Numerical results from the one-sixth model are used to compute the equivalent Darcy friction factor associated with fully developed flow conditions, whereas the outcomes from the CFD model including two complete turns are used to evaluate the concentrated loss coefficient related to the 180-degree turns. The equivalent Darcy friction factor of the channels is defined on the basis of the Darcy–Weisbach equation:

$$f_{D} = \frac{2\,\sigma_{fd}\, h_{ch}}{\rho\, \overline{u}_{I}^{2}}, \tag{23}$$

where $\overline{u}_{I}$ is the surface mean velocity over the inlet section of the channel. The term σ_{fd} stands for the external forcing maintaining the flow in the one-sixth channel model. The head losses associated with the 180-degree bends are expressed by a concentrated loss coefficient defined as:

$$\beta = \frac{2\,\Delta p_{bend}}{\rho\, \overline{u}_{I}^{2}}, \tag{24}$$

where, Δp_{bend}, the pressure drop caused by a single bend, is obtained by subtracting the distributed losses caused by the circular channels from the pressure difference Δp_{2t} driving the flow over two complete channel turns:

$$\Delta p_{bend} = \frac{1}{2}\left(\Delta p_{2t} - \frac{1}{2}\,\rho\, f_{D}\, \frac{l_{2t}}{h_{ch}}\, \overline{u}_{I}^{2}\right), \tag{25}$$

where l_{2t} is the curvilinear length of the channels across two complete turns:

$$l_{2t} = \frac{7}{2}\,\pi\left(r_{s,ext} + t_{a} + \frac{h_{ch}}{2}\right). \tag{26}$$

It is worth noting that in this way, additional losses in the channels caused by uneven flow distributions compared to the fully developed case are concentrated in the 180-degree bend. Nevertheless, this is common practice in networks of channels and pipes [63].

The aforementioned overall heat transfer and head losses figures are listed in Table 7 for a flow rate of a 50% by mass ethylene glycol-based coolant at Re = 2481, corresponding to a flow rate of 5 l/min. As it can be noted, extending the computational domain from one-sixth of a channel to two full revolutions results not only in an increase in head losses due to the presence of the 180-degree bends, but also in a noticeable decrease in the average Nusselt number values, due to the presence

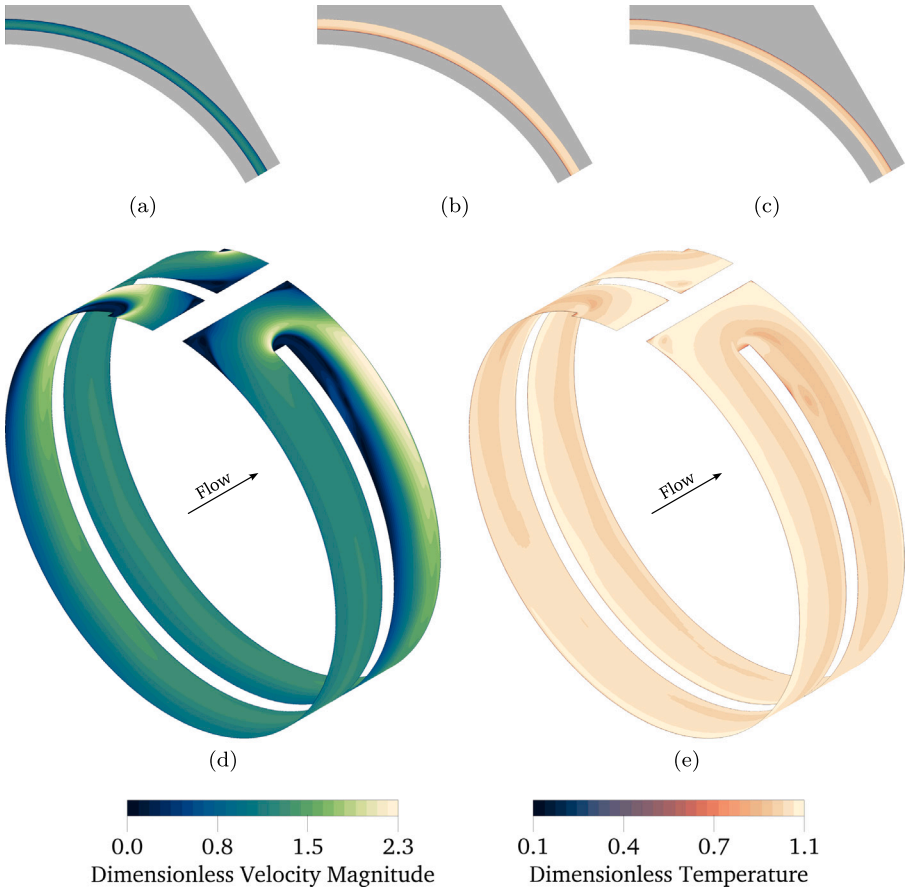

Fig. 11. Colour maps of dimensionless velocity magnitude and temperature difference as obtained by CFD. One-sixth of a channel: velocity field (a), temperature field (internal heating) (b), and temperature field (external heating) (c). Two channel turns: velocity field (d) and temperature field (internal heating) (e).

Table 7
Integral results on heat transfer and head losses obtained from the two CFD models developed for the cooling jacket. These are related to a flow rate of a 50% by mass ethylene glycol-based coolant at Re = 2481 (5 l/min).

Model	Nu_{int}	Nu_{ext}	f_D	β
one-sixth channel turn	21.3	20.1	0.029	
two channel turns	18.0	16.2		2.1

of recirculation regions and uneven flow distributions (see Fig. 11). In the case of the inner wall, the average Nu-value falls by 15% compared to the one-sixth results, whereas for the outer surfaces in contact with the converter boards, there is a 19% decrease in Nu. Although there is a significant difference between the heat transfer results produced by the two CFD models, it will be shown later that Nusselt number deviations of this magnitude have only a limited effect on the hot-spot temperatures of the motor and power converter components.

The overall head losses of the cooling jacket are evaluated as the sum of distributed losses over three complete turns of the channels, and the concentrated pressure drop given by two 180-degree bends:

$$\Delta p = \frac{1}{2}\,\rho\,\bar{u}_I^2\left(f_D\,\frac{1.5\,l_{2t}}{h_{ch}} + 2\,\beta\right) = 34.0\ \text{mbar}. \tag{27}$$

4.2. System-level results

4.2.1. Hot-spot temperatures

The system-level thermal models developed for the examined IMD, namely the 2D, 3D single-slot, and full 3D LPTNs are used to assess the feasibility of the proposed architecture from the thermal point of view. Table 8 reports the hot-spot temperature results associated with the three main components of the integrated assembly and related to the two different switch configurations considered for the power converter (worst-case and best-case conditions), which were discussed in Section 3.1. In addition, Table 8 lists the temperature limits of the windings, permanent magnets, and power semiconductors, along with their respective excess temperature values ΔT_{ex}, which are evaluated with respect to the coolant reference temperature considered for each thermal model, as in Table 4. Numerical temperature results seem to confirm the feasibility of the proposed integrated layout from the point of view of thermal management, as all hot-spot values are much lower than the thermal limit of their respective components.

The three thermal models produce comparable temperature results. According to both three-dimensional thermal models, adopting optimised power switches for the iFuse (best-case conditions) reduces the maximum junction temperature of up to 5 °C, while lesser improvements are reported by the 2D LPTN. As the electric motor and power converter are fully integrated, any enhancement in the thermal management of one device should also be reflected in the other. Indeed, this is the case according to both 3D thermal models, as the maximum winding temperatures decrease by two degrees when considering the best-case thermal scenario. The magnets are comparatively less affected, as the large equivalent thermal resistance between them and the cooling fluid dominates their thermal behaviour.

The two-dimensional thermal model does not highlight any of the aforementioned benefits, nor does it show any thermal interaction between the motor and power converter. However, this is fully expected, as by imposing a Dirichlet boundary condition for temperature at the node representing the mean coolant bulk temperature, the two devices are effectively uncoupled and behave as two separate systems subjected to equal temperature boundary conditions.

Table 8
Temperature limits and numerically obtained maximum temperature values in °C of the main components of the integrated motor drive. These temperature results are associated with Nu-values obtained from the CFD model of two complete channel turns. In this table, the worst-case and best-case conditions refer to the thermal loads associated with the non-optimised and optimised power switch configurations described in Section 3.1.

Model	Component	Temperature limit	Worst-case		Best-case	
			T_{max}	ΔT_{ex}	T_{max}	ΔT_{ex}
2D	Windings	180	117	48	117	48
	Magnets	310	185	116	185	116
	Converter	200	116	47	112	43
3D single-slot	Windings	180	132	72	130	80
	Magnets	310	194	134	192	132
	Converter	200	119	59	114	54
3D complete	Windings	180	129	69	127	67
	Magnets	310	192	132	190	130
	Converter	200	119	59	114	54

The temperature results in Table 8 were obtained by calculating the convective thermal resistances of the cooling jacket on the basis of the CFD model of two complete channel turns. This model accounts for the reduction in heat transfer effectiveness, compared to the CFD model of one-sixth of a channel, due to the presence of the 180-degree transitions between consecutive channels. By substituting the convective resistances computed from the one-sixth-channel model, the hot-spot temperatures decrease by 2 °C for all the components of the integrated assembly. These results, which are listed in Table A.10, highlight that, for the configuration under investigation, the dominant sources of thermal resistance, and thus the main contributors to hot-spot temperatures, are associated with heat conduction through the solid components of the motor and power converter, rather than convective heat transfer in the cooling jacket. Although the Nu-values associated with the cooling jacket increase by up to 19% when moving from the CFD model of two complete channel turns to that of a sixth of a single duct, no significant deviations in hot-spot temperatures are observed, or at least none that exceed the safety margins considered during the design of integrated motor drives and their cooling systems. Therefore, for preliminary assessments of different cooling jacket designs, it is sufficient to model the channels considering only one-sixth of their length, while more advanced CFD models can be employed to refine the results once the cooling system design has been finalised. This approach can significantly reduce computational cost, thereby reducing design lead times and costs.

The comparison between the two configurations considered for the power inverter is further expanded by evaluating the overall electrical efficiency of the integrated assembly. The latter is computed according to the diagram in Fig. 12, where L_{cn} and L_{mo} are the temperature-scaled losses of the power converter and electric motor, respectively. These are evaluated as follows:

$$L_{cn} = \sum_{l}^{n_{cn}} \dot{Q}_l \,, \quad L_{mo} = \sum_{l}^{n_{mo}} \dot{Q}_l \,, \tag{28}$$

where n_{cn} and n_m are the subsets of nodes associated with the converter and motor, respectively. Finally, the overall electrical efficiency is given by:

$$\eta = \eta_{cn}\,\eta_{mo} = \left(1 - \frac{L_{cn}}{P_{in}}\right)\left(1 - \frac{L_{mo}}{P_{in} - L_{cn}}\right). \tag{29}$$

Table 9 reports the efficiency values associated with the two configurations considered. In this case, the type of LPTN employed does not affect the efficiency results up to the third decimal place. Therefore, only one set of results is reported. The adoption of optimised semiconductors for the iFuses integrated in the switching cells improves the electrical efficiency of both the power converter and the overall integrated assembly by 0.7%. Overall, favouring a simpler, more straightforward chip-embedding process through the use of the same power device for the main and iFuse switches does not seem to bring forward significant penalties in terms of thermal management and efficiency. For this reason, the non-optimised configuration will be taken as a reference for the development of future prototypes of the power inverter.

Table 9
Electrical efficiency values according to Eq. (29).

Electrical efficiency	Worst case	Best case
η_{cn}	0.971	0.978
η_{mo}	0.975	0.976
η	0.947	0.954

In the following, the effects of modelling assumptions and methods on hot-spot temperature results are discussed further. On average, the T_{max}-values derived from the 2D LPTN are considerably lower than their counterparts from the 3D models. This is a somewhat expected behaviour since the 2D approach does not account for Joule effect losses in the end winding conductors. In addition, the assumption of a uniform coolant bulk temperature appears to yield lower overall temperatures in the rotor. The temperature values associated with the power converter are the least sensitive to the type of approach, as the converter boards are located towards the front of the motor where the coolant inlet is situated. As a result, the switching cells are less sensitive with respect to the coolant temperature increase along the axial direction.

The two 3D approaches produce comparatively similar results as both models consider all the losses associated with the assembly. These results also confirm the validity of the approach based on the parallel rule for the extension of the single-slot 3D model.

4.2.2. Temperature distributions

Fig. 13 shows temperature and heat flux distributions associated with the stator of the motor, obtained from the two-dimensional thermal network. These are obtained by using the `tricontourf` routine from the Matplotlib library [64], thereby plotting temperature values on an unstructured triangular grid defined by the coordinates of the temperature nodes. In this case, nineteen contour lines are visualised. In the active section of the motor, the hot-spot is located in correspondence of the first winding layer starting from the bottom. This is to be expected, as it features the largest equivalent thermal resistance to the cooling fluid. In the slot, the low thermal conductivity of the paper lining the surface favours heat conduction between adjacent winding layers, rather than between the copper bars and the stator teeth. As expected, the heat fluxes grow in value towards the external surface of the stator, as all the heat injected into the system is transferred to the cooling jacket. The largest $\dot{Q}$-value is observed at the centreline of the computational domain, as the thermal resistances in the centre encompass a larger surface area than those at the sides.

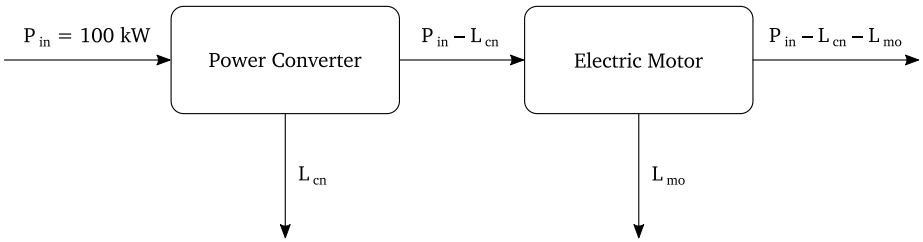

Fig. 12. Diagram representing the electrical power flow within the integrated motor drive, where the power entering the converter is P_{in} = 100 kW.

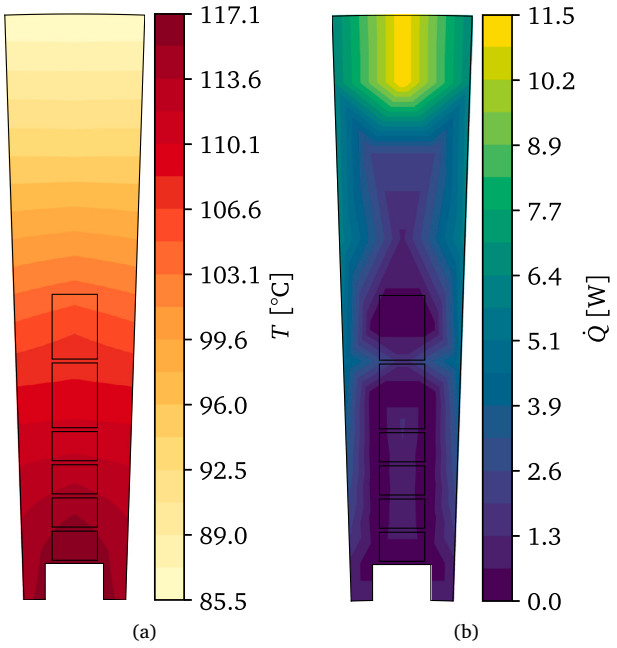

Fig. 13. Distributions of temperature (a) and heat fluxes (b), obtained from the two-dimensional LPTN and considering the non-optimal converter configuration.

Table 8 presents a close agreement between numerical results from the 3D LPTNs, when considering hot-spot temperature values. However, the situation changes slightly when taking into account the temperature distribution across the entire winding assembly. Fig. 14 shows the temperature distributions of all six winding layers along the axial direction z, and obtained from both the 3D LPTNs. In the case of the complete 3D LPTN, this distribution is obtained by averaging winding temperatures along the circumferential direction, in order to make a fair comparison with the outcomes of the single-slot 3D approach. As previously stated, both models produce similar hot-spot winding temperatures in correspondence of the first end winding layer at the back of the motor, where numerical results from the complete 3D LPTNs underestimate those from the 3D single-slot model by around 3 °C. However, a steeper temperature gradient $\partial T/\partial z$ is noted in the case of the full 3D model, leading to larger temperature differences between the two models towards the front of the motor and across all winding layers. This suggests that the redistribution of heat fluxes across winding layers through the end windings has a substantial impact, and contributes towards the reduction of winding temperatures at the front of the motor and in the active section.

Fig. 15 reports a contour plot of the temperature distribution of both stator and rotor on a transversal cross-section at the centreline of the motor. This plot is obtained using the same procedure employed for the contour plots in Fig. 13. In the stator, an analogous temperature distribution to that observed in Fig. 13(a) is noted, while circumferential heat conduction and the coolant temperature increase do not appear to result in significant azimuthal temperature gradients. The rotor presents a much more uniform temperature distribution, due to reduced losses compared to the stator, and a greater uniformity in terms of constitutive materials.

In conclusion, the 3D single-slot thermal model represents the best compromise between complexity and accuracy for the computation of hot-spot temperatures as it constitutes a direct improvement over the 2D LPTN, while not requiring the same development and computational effort as the complete 3D model. Furthermore, the lack of significant circumferential temperature gradients in Fig. 15 reinforces the effectiveness of the 3D single-slot model. Finally, despite the minor differences noted in the computed winding temperatures between the full 3D and 3D single-slot models, the latter produces results that favour safety from a thermal perspective.

In addition, if a more faithful representation of the temperature distribution is sought, the 3D LPTN should be used instead. Still, the 2D model represents a very simple approach to obtain rapid and fairly accurate evaluations on the thermal performance of the machine, especially for the magnets and power converter, while moderate deviations should be expected for the windings.

5. Concluding remarks

The present work investigated the thermal management of a novel integrated motor drive design, presenting PCB-embedded SiC MOSFETs included in a multilevel power converter with a switching cell array architecture. This design is an improvement over traditional architectures as it avoids the thermal limitations associated with conventionally packaged power devices. The study was carried out by developing three multiscale thermal models based on lumped parameter thermal networks, capable of capturing the thermal coupling between motor and inverter. In these models, the heat sources and relevant thermal resistances were defined on the basis of numerical results from Finite Element and Computational Fluid Dynamics models. The latter was specifically developed to evaluate the heat transfer coefficients associated with the cooling jacket.

Temperature results from the three thermal models were compared, discussing the strengths and weaknesses of each approach, with the aim of providing guidelines for the selection of modelling approaches suitable for real design workflows. As expected, the 2D LPTN produced the lowest hot-spot temperatures due to the absence of end winding losses and the assumption of a uniform coolant bulk temperature throughout the whole cooling jacket. In this case, the windings reached a maximum temperature of 117 °C, while the magnets and power electronic device presented hot-spots of 185 °C and 116 °C, respectively. The optimised power switch configuration decreased the power converter hot-spot by 4 °C. However, this did not benefit the electric motor, as in the 2D model the two subsystems were thermally uncoupled.

Both the 3D thermal models provided close estimations for the hot-spot temperatures in the windings, rotor, and power converter. The 3D single slot model produced the highest temperature figures for the motor, with winding temperatures of up to 132 °C and magnet temperatures of up to 194 °C. Regarding the converter, the two 3D models

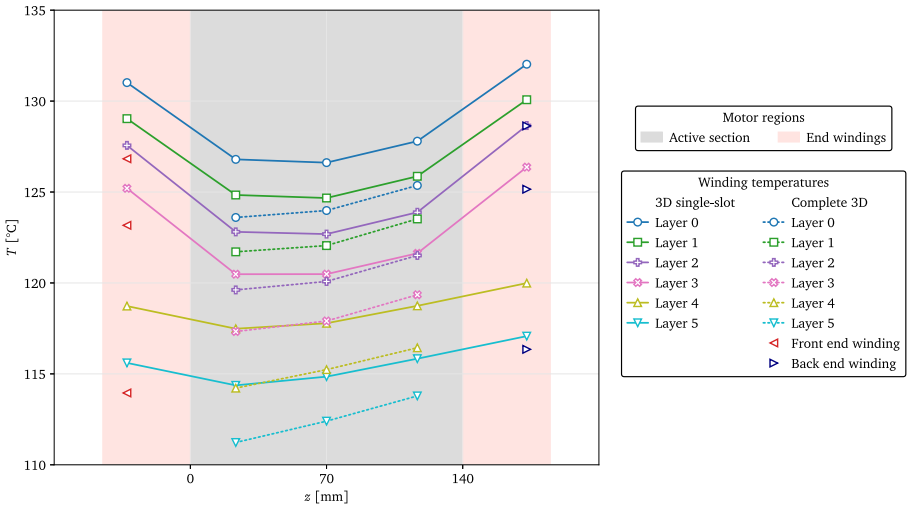

Fig. 14. Distributions of winding temperatures along the axis of the electric motor, obtained from the 3D single-slot model (solid lines) and complete 3D LPTN (dotted lines), while considering the worst-case thermal scenario.

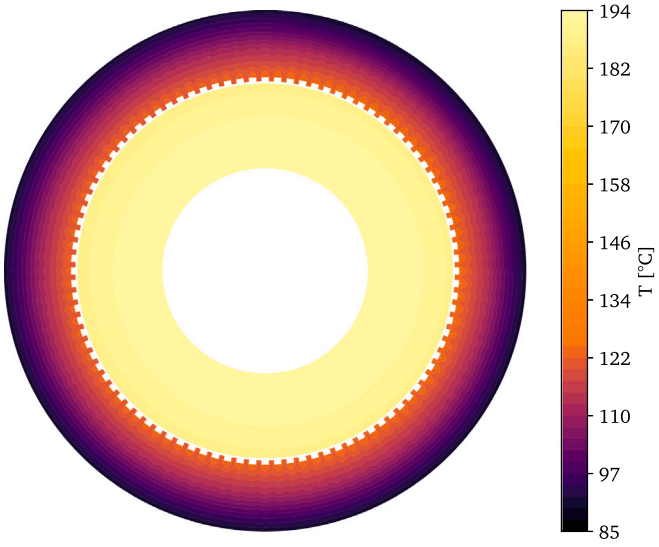

Fig. 15. Temperature contour plot of the stator and rotor obtained on a cross-section located at the centre of the motor, considering numerical results from the complete 3D thermal model.

produced equal hot-spot temperature figures. In this instance, the thermal coupling between motor and power converter was evident, as the optimised power device configuration decreased hot-spot temperatures in the motor by 2 °C for both the windings and magnets. The hot-spot temperatures of the most relevant components were well below their respective thermal limits, proving the effectiveness of the proposed architecture. Finally, the temperature-corrected losses resulting from the thermal models were included in the overall electrical efficiency computation, resulting in a maximum efficiency value of 95.4%.

The large increase in the number of degrees of freedom in the full 3D model compared to the 3D axial one mostly affected the temperature gradients along the axial direction of the machine, and the distribution of winding temperatures. Thus, the simplified three-dimensional LPTN appears to offer the optimal balance between computational effort and accuracy regarding the computation of the hot-spots, making it the most suitable approach to rapidly evaluate different design variants in fast-paced industrial settings. The results presented in this work highlight the potential of PCB-embedded power devices to improve the integration and thermal management of integrated motor drives.

CRediT authorship contribution statement

Mattia Grespan: Conceptualization, Methodology, Software, Validation, Formal analysis, Investigation, Data curation, Writing – original draft, Writing – review & editing . **Sergio Busquets-Monge:** Resources, Writing – review & editing, Supervision, Project administration. **Elisabet Mas de les Valls:** Supervision. **Salvador Alepuz:** Resources, Writing – review & editing. **Mariana Raya:** Resources. **Xavier Jordà:** Writing – review & editing, Resources. **Davide Barater:** Writing – review & editing, Resources, Supervision, Project administration. **Diego Angeli:** Writing – review & editing, Supervision, Project administration.

Declaration of competing interest

The authors declare that they have no known competing financial interests or personal relationships that could have appeared to influence the work reported in this paper.

Acknowledgements

This research was funded by the European Union's Horizon Europe research and innovation program under grant agreement No. 101056781. Views and opinions expressed are however those of the authors only and do not necessarily reflect those of the European Union or CINEA. Neither the European Union nor the granting authority can be held responsible for them.

Appendix. Additional hot-spot temperature results

See Table A.10.

Data availability

The data that has been used is confidential.

Table A.10
Temperature limits and numerically obtained maximum temperature values in °C of the main components of the integrated motor drive. These temperature results are associated with Nu-values obtained from the CFD model of one-sixth of a single channel. In this table, the worst-case and best-case conditions refer to the thermal loads associated with the non-optimised and optimised power switch configurations described in Section 3.1.

Model	Component	Temperature limit	Worst-case		Best-case	
			T_{max}	ΔT_{ex}	T_{max}	ΔT_{ex}
2D	Windings	180	115	46	115	46
	Magnets	310	183	114	183	114
	Converter	200	113	45	110	41
3D single-slot	Windings	180	130	70	128	68
	Magnets	310	192	132	190	130
	Converter	200	117	58	112	52
3D complete	Windings	180	127	67	125	65
	Magnets	310	190	129	188	128
	Converter	200	116	56	112	52

References

[1] T.M. Jahns, H. Dai, The past, present, and future of power electronics integration technology in motor drives, CPSS Trans. Power Electron. Appl. 2 (3) (2017) 197–216.

[2] M. Bradfield, Thermal design challenges in automotive alternator power electronics, Electron. Cool. 8 (2002) 28–33.

[3] H. Shimizu, T. Okubo, I. Hirano, S. Ishikawa, M. Abe, Development of an Integrated Electrified Powertrain for a Newly Developed Electric Vehicle, Technical Report, SAE Technical Paper, 2013.

[4] K. Suzuki, K. a Yuki, M. Mochizuki, Application of boiling heat transfer to high-heat-flux cooling technology in power electronics, Trans. Jpn. Inst. Electron. Packag. 4 (1) (2011) 127–133.

[5] C. Wang, D. Li, R. Qu, X. Fan, W. Kong, H. Fang, Z. Gao, P. Yan, A combined thermal analysis of an integrated six-phase motor drive system, in: 2018 IEEE Energy Conversion Congress and Exposition, ECCE, 2018, pp. 4323–4328.

[6] S. Pickering, P. Wheeler, F. Thovex, K. Bradley, Thermal design of an integrated motor drive, in: IECON 2006–32nd Annual Conference on IEEE Industrial Electronics, 2006, pp. 4794–4799.

[7] R. Abebe, G. Vakil, G. Lo Calzo, T. Cox, C. Gerada, M. Johnson, Fea based thermal analysis of various topologies for integrated motor drives (imd), in: IECON 2015–41st Annual Conference of the IEEE Industrial Electronics Society, 2015, pp. 001976–001981.

[8] O.S. Chaudhary, M. Denaï, S.S. Refaat, G. Pissanidis, Technology and applications of wide bandgap semiconductor materials: Current state and future trends, Energies 16 (18) 2023.

[9] K. Chen, W. Feng, F. Chen, S. Lee, J. Paddock, T.M. Jahns, B. Sarlioglu, Thermal analysis of liquid and air cooling of high-power-density integrated motor drives, in: 2023 IEEE Energy Conversion Congress and Exposition, ECCE, 2023, pp. 4487–4493.

[10] F. Tokgoz, Ö. Gülsuna, F. Karakaya, G. Cakal, O. Keysan, Mechanical and thermal design of an optimized pcb motor for an integrated motor drive system with ganfets, IEEE Trans. Energy Convers. 38 (1) (2023) 653–661.

[11] R.L. Kotnik, Equivalent thermal circuit for nonventilated motors, Electr. Eng. 74 (3) (1955) 213.

[12] D.R. Turner, P.H. Mellor, D. Roberts, Lumped parameter thermal model for electrical machines of tefc design, in: Proceedings of the Institution of Electrical Engineers - Electrical Power Applications, vol. 138, (13) 1991, pp. 205–218.

[13] S.K. Chowdhury, P.K. Baski, A simple lumped parameter thermal model for electrical machine of tefc design, in: 2010 Joint International Conference on Power Electronics, Drives and Energy Systems 2010 Power India, 2010, pp. 1–7.

[14] C. Kral, A. Haumer, T. Bauml, Thermal model and behavior of a totally-enclosed-water-cooled squirrel-cage induction machine for traction applications, IEEE Trans. Ind. Electron. 55 (10) (2008) 3555–3565.

[15] T. Bauml, C. Kral, A. Haumer, H. Kapeller, Enhanced thermal model of a totally enclosed fan cooled squirrel cage induction machine, in: 2007 IEEE International Electric Machines Drives Conference, vol. 2, 2007, pp. 1054–1058.

[16] F. Ahmed, E. Ghosh, N.C. Kar, Transient thermal analysis of a copper rotor induction motor using a lumped parameter temperature network model, in: 2016 IEEE Transportation Electrification Conference and Expo, ITEC, 2016, pp. 1–6.

[17] O. Aglen, A. Andersson, Thermal analysis of a high-speed generator, in: 38th IAS Annual Meeting on Conference Record of the Industry Applications Conference, 2003 volume 1, vol. 1, 2003, pp. 547–554.

[18] A.M. EL-Refaie, N.C. Harris, T.M. Jahns, K.M. Rahman, Thermal analysis of multibarrier interior pm synchronous machine using lumped parameter model, IEEE Trans. Energy Convers. 19 (2) (2004) 303–309.

[19] P. Ponomarev, M. Polikarpova, J. Pyrhönen, Thermal modeling of directly-oil-cooled permanent magnet synchronous machine, in: 2012 XXth International Conference on Electrical Machines, 2012, pp. 1882–1887.

[20] A. Boglietti, A. Cavagnino, M. Lazzari, A. Pastorelli, A simplified thermal model for variable speed self cooled industrial induction motor, in: Conference Record of the 2002 IEEE Industry Applications Conference. 37th IAS Annual Meeting (Cat. No. 02CH37344). volume 2, vol. 2, 2002, pp. 723–730.

[21] G. Henneberger, K.B. Yahia, M. Schmitz, Calculation and identification of a thermal equivalent circuit of a water cooled induction motor for electric vehicle applications, in: 1995 Seventh International Conference on Electrical Machines and Drives (Conf. Publ. No. 412), 1995, pp. 6–10.

[22] O. Wallscheid, J. Böcker, Global identification of a low-order lumped-parameter thermal network for permanent magnet synchronous motors, IEEE Trans. Energy Convers. 31 (1) (2016) 354–365.

[23] C. Sciascera, P. Giangrande, L. Papini, C. Gerada, M. Galea, Analytical thermal model for fast stator winding temperature prediction, IEEE Trans. Ind. Electron. 64 (8) (2017) 6116–6126.

[24] B. Guo, Y. Huang, Y. Guo, J. Zhu, Thermal analysis of the conical rotor motor using lptn with accurate heat transfer coefficients, IEEE Trans. Appl. Supercond. 26 (7) (2016) 1–7.

[25] S. Nategh, Z. Huang, A. Krings, O. Wallmark, M. Leksell, Thermal modeling of directly cooled electric machines using lumped parameter and limited cfd analysis, IEEE Trans. Energy Convers. 28 (4) (2013) 979–990.

[26] F. Ahmed, P. Roy, M. Towhidi, G. Feng, Narayan C. Kar, Cfd and lptn hybrid technique to determine convection coefficient in end-winding of tefc induction motor with copper rotor, in: IECON 2019–45th Annual Conference of the IEEE Industrial Electronics Society, vol. 1, 2019, pp. 939–944.

[27] M.H. Park, S.C. Kim, Development and validation of lumped parameter thermal network model on rotational oil spray cooled motor for electric vehicles, Appl. Therm. Eng. 225 (2023) 120176.

[28] S. Mezani, N. Takorabet, B. Laporte, A combined electromagnetic and thermal analysis of induction motors, IEEE Trans. Magn. 41 (5) (2005) 1572–1575.

[29] O.I. Okoro, Steady and transient states thermal analysis of a 7.5-kw squirrel-cage induction machine at rated-load operation, IEEE Trans. Energy Convers. 20 (4) (2005) 730–736.

[30] J. Fan, C. Zhang, Z. Wang, Y. Dong, C.E. Nino, A.R. Tariq, E.G. Strangas, Thermal analysis of permanent magnet motor for the electric vehicle application considering driving duty cycle, IEEE Trans. Magn. 46 (6) (2010) 2493–2496.

[31] L. Alberti, N. Bianchi, A coupled thermal-electromagnetic analysis for a rapid and accurate prediction of im performance, IEEE Trans. Ind. Electron. 55 (10) (2008) 3575–3582.

[32] G. Dajaku, D. Gerling, An improved lumped parameter thermal model for electrical machines, in: 17th International Conference on Electrical Machines (ICEM2006), Citeseer, 2006, pp. 1–6.

[33] D. Gerling, G. Dajaku, Thermal calculation of systems with distributed heat generation, in: Thermal and Thermomechanical Proceedings 10th Intersociety Conference on Phenomena in Electronics Systems, 2006. ITHERM 2006., 2006, pages 8 pp. –652.

[34] D. Gerling, G. Dajaku, Novel lumped-parameter thermal model for electrical systems, in: 2005 European Conference on Power Electronics and Applications, 2005, pages 10 pp. –P.10.

[35] C.H. van der Broeck, M. Conrad, R.W. De Doncker, A thermal modeling methodology for power semiconductor modules, Microelectron. Reliab. 55 (9) (2015) 1938–1944, Proceedings of the 26th European Symposium on Reliability of Electron Devices, Failure Physics and Analysis.

[36] M. März, P. Nance, Thermal modeling of power electronic systems, Infineon Technol. AG Munich 2, 2000.

[37] C. Qian, A.M. Gheitaghy, J. Fan, H. Tang, B. Sun, H. Ye, G. Zhang, Thermal management on igbt power electronic devices and modules, IEEE Access 6 (2018) 12868–12884.

[38] A. Lakhsasi, Y. Hamri, A. Skorek, Partially coupled electro-thermal analysis for accurate prediction of switching devices, in: Canadian Conference on Electrical and Computer Engineering 2001. Conference Proceedings (Cat. No. 01TH8555). volume 1, vol. 1, 2001, pp. 375–380.

[39] S. Busquets-Monge, L. Caballero, Switching-cell arrays–an alternative design approach in power conversion, IEEE Trans. Ind. Electron. 66 (1) (2019) 25–36.
[40] S. Alepuz, J. Nicolás-Apruzzese, G. García-Rojas, S. Busquets-Monge, M. Grespan, X. Yuan, Thermal stress reduction in neutral-point-clamped multilevel converters through a switching-cell array-based implementation and active thermal control, Electronics 15 (5) 2026.
[41] M. Pastura, R. Notari, S. Nuzzo, D. Barater, G. Franceschini, Ac losses analysis and design guidelines for hairpin windings with segmented conductors, IEEE Trans. Transp. Electrific. 10 (1) (2024) 33–41.
[42] M. Raya, E. Solà, M. Vellvehi, X. Perpiñà, P. Lasserre, S. Busquets-Monge, X. Jordà, Sic mosfet chip embedded switching-cell for multilevel converters, in: IEEE 37th International Symposium on Power Semiconductor Devices and ICs, ISPSD, 2025.
[43] Y. Sato, S. Ishikawa, T. Okubo, M. Abe, K. Tamai, Development of High Response Motor and Inverter System for the Nissan Leaf Electric Vehicle, Technical Report, SAE Technical Paper, 2011.
[44] M. Grespan, S. Busquets-Monge, E. Mas DeLesValls, X. Jordà, M.R. DiFrancisco, D. Angeli, Thermal analysis of an integrated motor drive with a switching cell array power converter, J. Phys.: Conf. Ser. 2766 (2024) 012033, IOP Publishing.
[45] M. Yovanovich, A general expression for predicting conduction shape factors, in: 11th AIAA Aerospace Sciences Meeting, 1973.
[46] D. Staton, A. Boglietti, A. Cavagnino, Solving the more difficult aspects of electric motor thermal analysis in small and medium size industrial induction motors, IEEE Trans. Energy Convers. 20 (3) (2005) 620–628.
[47] I.S. Bjorklund, W.M. Kays, Heat transfer between concentric rotating cylinders, J. Heat Transf. 81 (3) (1959) 175–183, 08.
[48] R. Wrobel, A. Griffo, P.H. Mellor, Scaling of ac copper loss in thermal modeling of electrical machines, in: 2012 XXth International Conference on Electrical Machines, 2012, pp. 1424–1429.
[49] M. Pastura, R. Notari, S. Nuzzo, D. Barater, G. Franceschini, Ac losses analysis and design guidelines for hairpin windings with segmented conductors, IEEE Transactions Transportation Electrific (2023) 1.
[50] M. Pastura, R. Notari, S. Nuzzo, D. Barater, G. Franceschini, On the ac losses in the end conductors of hairpin windings, in: 2022 International Conference on Electrical Machines, ICEM, 2022, pp. 1150–1155.
[51] R. Rafiezadeh, S. Busquets-Monge, S. Alepuz, Thermo-electrical modeling of multilevel switching-cell-array-based power converters, in: 2023 IEEE 32nd International Symposium on Industrial Electronics, ISIE, 2023, pp. 1–8.
[52] F. Zhang, et al., A thermal modeling approach and experimental validation for an oil spray-cooled hairpin winding machine, IEEE Trans. Transp. Electrific 7 (4) (2021) 2914–2926.
[53] S. Nalakath, M. Preindl, B. Bilgin, B. Cheng, A. Emadi, Modeling and analysis of ac resistance of a permanent magnet machine for online estimation purposes, in: 2015 IEEE Energy Conversion Congress and Exposition, ECCE, 2015, pp. 314–319.
[54] A. Boglietti, A. Cavagnino, D.A. Staton, M. Popescu, Impact of different end region cooling arrangements on endwinding heat transfer coefficients in electric motors, in: 2009 35th Annual Conference of IEEE Industrial Electronics, 2009, pp. 1168–1173.
[55] P. Virtanen, et al., SciPy 1.0: Fundamental Algorithms for Scientific Computing in Python, Nature Methods 17 (2020) 261–272.
[56] M. Grespan, L. Calò, L. Carlesso, A. Leonforte, D. Angeli, A comprehensive numerical study on heat transfer and friction characteristics of offset-strip fins, Appl. Therm. Eng. 256 (2024) 124083.
[57] F.R. Menter, Two-equation eddy-viscosity turbulence models for engineering applications, AIAA J. 32 (8) (1994) 1598–1605, Cited by: 13968; All Open Access, Green Open Access..
[58] M. Grespan, A. Leonforte, L. Calò, M. Cavazzuti, D. Angeli, Physics-based modelling of plate-fin heat exchangers, Energies 18 (3) 2025.
[59] S.V. Patankar, D.B. Spalding, A calculation procedure for heat, mass and momentum transfer in three-dimensional parabolic flows, in: Numerical Prediction of Flow, Heat Transfer, Turbulence and Combustion, Elsevier, 1983, pp. 54–73.
[60] H.G. Weller, G. Tabor, H. Jasak, C. Fureby, A tensorial approach to computational continuum mechanics using object-oriented techniques, Comput. Phys. 12 (6) (1998) 620–631.
[61] P.D. Thomas, J.F. Middlecoff, Direct control of the grid point distribution in meshes generated by elliptic equations, AIAA J. 18 (6) (1980) 652–656.
[62] P.J. Roache, Quantification of uncertainty in computational fluid dynamics, Annu. Rev. Fluid Mech. 29 (1) (1997) 123–160.
[63] M.J. Moran, H.N. Shapiro, D.D. Boettner, M.B. Bailey, B.R. Munson, D.P. DeWitt, M. A Corticelli, et al., Elementi di fisica tecnica per l'ingegneria II edizione, McGraw-Hill education, 2022.
[64] J.D. Hunter, Matplotlib: A 2d graphics environment, Comput. Sci. Eng. 9 (3) (2007) 90–95.